

# Structure and thermodynamics of platelet dispersions

L. Harnau

*Max-Planck-Institut für Metallforschung, Heisenbergstr. 3, D-70569 Stuttgart, Germany,  
and Institut für Theoretische und Angewandte Physik,  
Universität Stuttgart, Pfaffenwaldring 57, D-70569 Stuttgart, Germany*

Various properties of fluids consisting of platelike particles differ from the corresponding ones of fluids consisting of spherical particles because interactions between platelets depend on their mutual orientations. One of the main issues in this topic is to understand how structural properties of such fluids depend on factors such as the shape of the platelets, the size polydispersity, the orientational order, and the platelet number density. A statistical mechanics approach to the problem is natural and in the last few years there has been a lot of work on the study of properties of platelet fluids. In this contribution some recent theoretical developments in the field are discussed and experimental investigations are described.

## I. INTRODUCTION

The symmetry of the shape of platelike particles is reduced compared with spherical symmetry so that interactions between them depend not only on the separation between their centers but also on their mutual orientations. As a result pair correlation functions and phase diagrams of fluids consisting of such particles differ from the corresponding ones of fluids consisting of spherical particles. In this article various properties of platelet fluids are discussed. The structure of the article is as follows. In Section II some examples of platelet fluids including the experimental investigations are presented. The knowledge about the shape of the particles and their size polydispersity allows one to calculate intermolecular pair correlation functions and the equation of state in the isotropic phase within the framework of an interaction site integral equation theory as is discussed in Sections III and IV. The theoretically obtained static structure factor and isothermal compressibility are compared with experimental data. Density functional theory is used in Section V to study orientational order in spatially homogeneous bulk phases. Moreover, some brief details about properties of platelet fluids in contact with substrates are recorded. Some aspects of spatially inhomogeneous bulk phases are discussed in Section VI. Finally, Section VII draws conclusions.

## II. SHAPE OF PARTICLES AND POLYDISPERSITY IN SIZE

In the following we will present examples of systems that illustrate the range of interest in platelet dispersions. The shape of the particles and the polydispersity in size can be revealed by cryogenic transmission electron microscopy and scattering methods.

### A. Cryogenic transmission electron microscopy of polyethylene nanoplatelets

Polyethylene is a commodity polymer that has become ubiquitous over the past several decades because of its low price and good mechanical properties. Hence, the number of applications of the material is huge and many millions of tons are produced worldwide annually. However, polyethylene has hardly played any role in the field of nanotechnology. This is due to the problem that polyethylene is produced either by free radical polymerization under high pressure and temperature or with metal-organic catalysts working exclusively under strictly water-free conditions. Polymer nanoparticles and their composites with inorganic compounds, however, are very often produced in aqueous systems. Recently, it has been demonstrated that ethylene can be polymerized in aqueous systems in a catalytic fashion by Ni(II) complexes. By virtue of this novel synthesis, long chains of polyethylene can be generated in a well-controlled environment and at ambient temperature. Thus, it could be shown that aqueous polyethylene dispersions can be produced. This polymerization has opened the way of well-defined polyethylene nanoplatelets consisting of the smallest single crystal of polyethylene ever reported [1]. Semi-crystalline polyethylene in extremely mild conditions of pressure and temperature have been prepared. During this process, nanoplatelets exclusively made of polyethylene are formed by the chains as soon as they polymerize. In principle, the crystallization could start while the chains are still growing. However, the fast polymerization process and the slow nucleation in confined nanoparticles prevent the crystallization from starting before the whole particle is formed. It is thus a melt crystallization that takes place in each nanoplatelet with an extraordinary degree of supercooling which could not be achieved by any other method [2].

Specimens for cryogenic transmission electron microscopy (cryo-TEM) have been prepared by vitrification of a thin liquid film of the diluted dispersion supported by a copper grid in liquid ethane. Figure 1 displays a micrograph of the particles in dilute aqueous solution as

obtained by cryo-TEM. The dispersion consists of flat platelets. The different gray scales for different particles can be easily rationalized by different viewing angles: If the normal of a platelet is nearly perpendicular to the electron beam, the length of the optical path through the particles is much longer than for parallel arrangement. The platelets have a hexagonal shape with rather straight edges. From cryo-TEM images a lateral dimension (pseudo-diameter) of  $25.4 (\pm 4.3)$  nm and a corresponding thickness of the platelets of  $6.3 (\pm 0.8)$  nm have been determined [1]. The observed nanoplatelets can be considered as single lamellae of polyethylene. The crystallinity of the nanoplatelets has been confirmed by wide-angle x-ray scattering measurements performed on the dispersion. The crystalline lamellae visible in Fig. 1 are expected to be covered by an amorphous layer as polyethylene is a semicrystalline polymer. However, it is not possible to detect this by cryo-TEM. This is due to the fact that the electron density of amorphous polyethylene is virtually the same as that of the low density amorphous ice. Hence, there is not a sufficient contrast between a possible amorphous layer and the surrounding medium. However, this problem can be treated by applying contrast variation small-angle x-ray scattering as an analytical tool as is outlined in the following subsection. Figure 1 also demonstrates that the particles are well-dispersed in the aqueous medium; virtually no aggregates are found. This is a prerequisite for a meaningful investigation by scattering methods in solution.

Cryo-TEM has also been used to analyze the shape and size polydispersity of larger colloidal platelets such as nickel hydroxide  $[\text{Ni}(\text{OH})_2]$  platelets of 180 nm diameter and 10 nm thickness [3, 4] as well as gibbsite  $[\text{Al}(\text{OH})_3]$  platelets of 200 nm diameter and 15 nm thickness [5, 6, 7, 8, 9, 10, 11, 12, 13, 14, 15, 16, 17, 18, 19, 20]. However, a quantitative determination of the thickness of these colloidal platelets in solution is not straightforward, because in particular thin platelets can hardly ever be viewed edgewise on TEM images, while very thick platelets touching the TEM grid with their rim have been found. The influence of confining surfaces on the orientation of the platelets was also discovered in suspensions of Ag, Ni, and  $\text{Fe}_x\text{Ni}_{1-x}$  nanoplatelets [21, 22, 23, 24]. In order to promote the edgewise orientation of platelets on the TEM grid one may use deliberately flocculated samples [10]. The fact that the domains of liquid-crystalline phases of colloidal platelets at higher particle number densities extend over rather large distances is also due to the influence of the rigid walls of the sample cells.

## B. Scattering methods

The theory of static scattering has been presented in various books. Here, we review the results necessary for this study. Light scattering, small-angle neutron scattering, and small-angle x-ray scattering determine the scattering intensity  $I(\mathbf{q}, \rho)$  as a function of the scattering

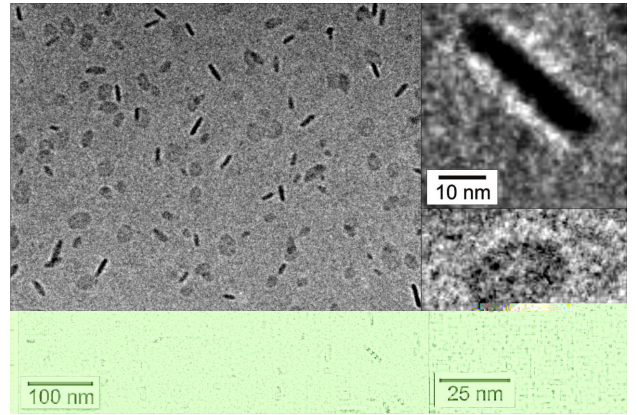


FIG. 1: Cryogenic transmission electron microscopy micrograph of polyethylene nanoplatelets in aqueous dispersion [1]. The grey background is the low-density amorphous ice in which the particles are dispersed. The particles are flat platelets, appearing as rods when their normal is perpendicular to the electron beam (upper inset) and hexagons when their normal is rather parallel to the electron beam (lower inset).

vector  $\mathbf{q}$  and the number density of the dissolved particles  $\rho$ . The absolute value of the scattering vector is given by  $q = |\mathbf{q}| = (4\pi n/\lambda) \sin(\theta/2)$  in which  $n$  is the refractive index of the medium,  $\lambda$  is the incident wavelength, and  $\theta$  is the scattering angle. The scattering intensity can be written as

$$I(\mathbf{q}, \rho) = \rho I_0(\mathbf{q}) S(\mathbf{q}, \rho) + \rho I_{incoh}, \quad (1)$$

where  $I_0(\mathbf{q})$  is the scattering intensity of a single particle,  $S(\mathbf{q}, \rho)$  is the structure factor related to the mutual interactions of the solute particles, and  $I_{incoh}$  is the incoherent contribution in small-angle neutron scattering that is mainly due to the hydrogen atoms of the particles. The incoherent contribution  $I_{incoh}$  must be subtracted carefully from experimental data in order to obtain meaningful results on the structure and interaction of the dissolved particles. There is no such contribution in light scattering and small-angle x-ray scattering. The scattering intensity of a single particle may be used to define the form factor  $P(\mathbf{q})$  that is normalized to unity at  $q = 0$  according to

$$I_0(\mathbf{q}) = V_p^2 (\Delta\tilde{\rho})^2 P(\mathbf{q}), \quad (2)$$

where  $V_p$  is the volume of a dissolved particle and  $\Delta\tilde{\rho}$  is the contrast of the solute resulting from the difference of the average scattering length density of the dissolved particles and the scattering density of the solvent. In the case of light scattering and small-angle x-ray scattering, the contrast is fixed by the solvent, the partial specific volume of the solute, and its chemical composition. In the case of small-angle neutron scattering,  $\Delta\tilde{\rho}$  is

an available model parameter that can be varied by mixing protonated and deuterated solvent. The form factor of randomly oriented monodisperse circular platelets of radius  $R$  and thickness  $L$  is given by

$$P(q) = 4 \int_0^1 dx \frac{J_1^2(qR\sqrt{1-x^2}) \sin^2(qLx/2)}{(qR\sqrt{1-x^2})^2 (qLx/2)^2}, \quad (3)$$

where  $J_1(x)$  denotes the cylindrical Bessel function of first-order. The effect of size polydispersity of the platelets is taken into account by an appropriate average according to

$$\langle I_0(\mathbf{q}) \rangle = \int_0^\infty dR \int_0^\infty dL I_0(\mathbf{q}) G(R, L), \quad (4)$$

where  $G(R, L)$  is a distribution function characterizing the degree of polydispersity.

### 1. Form factor of stilbenoid dendrimers

Dendrimers are synthetic macromolecules with defined architecture that are synthesized by iterative controlled reaction steps. Starting from a focal unit, subsequent generations are connected to this initial core which results in a treelike structure. Dendrimers composed of flexible units adopt a so-called dense core structure characterized by an average segmental density that has its maximum at the center of the molecule. This is easily derived from the fact that flexible dendrimers can assume a great number of conformations in which the terminal groups can fold back. Hence these flexible dendrimers do not exhibit a well-defined surface given by the terminal groups of the last generation. The average density profile thus derived can be used to calculate the interaction of flexible dendrimers in solution. These structures are well understood by now [25]. Much less attention has been paid to dendrimers consisting of rigid units [26, 27, 28, 29, 30, 31, 32, 33, 34]. Figure 2 shows the chemical structure of a rigid stilbenoid dendrimer of the third generation which is solely composed of stiff units. Starting from a central phenyl group, all subsequent generations are built up by trans-stilben units, only the terminal groups are substituted by hexyloxy groups in order to ensure better solubility in common solvents such as toluene. Full conjugation in trans-stilbene can be achieved in the completely planar conformation. However, the potential energy for a slight torsion around the single bonds is low in the ground state of trans-stilbene. Molecular modeling without taking into account the solvent has demonstrated that a stilbenoid dendrimer of the third generation exhibits a relatively compact platelike structure [28].

The spatial structure of the stilbenoid dendrimers in dilute solution has been investigated by small-angle x-ray scattering and small-angle neutron scattering [35]. Both

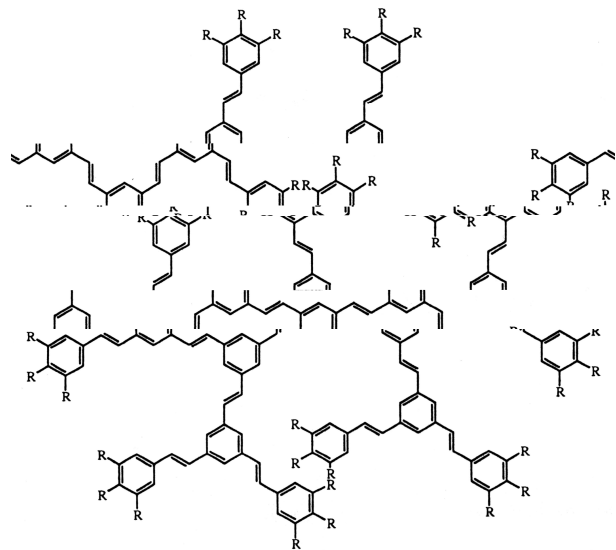


FIG. 2: Chemical structure of a stilbenoid dendrimer of the third generation ( $R = OC_6H_{13}$ ).

methods give different information: Small-angle neutron scattering data taken at high contrast between the solute and the solvent can be used to explore the shape of the entire molecule. Small-angle x-ray scattering, however, is mainly sensitive to the stilbenoid scaffold of the molecule and hardly detects the hydrocarbon chains attached to its periphery due to the fact that these hexyl chains are virtually matched by the solvent toluene.

The form factor  $P(q)$  of stilbenoid dendrimers of the third generation as obtained by small-angle neutron scattering is shown in Fig. 3. The form factor agrees with the one calculated numerically for a monodisperse circular platelet with a radius  $R = 2.4$  nm and thickness  $L = 1.8$  nm according to Eq. (3). The good agreement between the experimental and theoretical results demonstrates that a full understanding of the spatial structure of stilbenoid dendrimers of the third generation has been achieved [35]. Dendrimers consisting of rigid units exhibit a rather well defined structure in solution and may serve as model systems for interacting monodisperse particles in statistical physics [36] as is discussed in Section IV.

### 2. Form factor of laponite platelets

Laponite consists of platelike clay particles with a radius  $R \approx 11.5$  nm and thickness  $L \approx 0.9$  nm. Each platelet carries a few hundred elementary charges. For a long time, aqueous suspensions of laponite have been extensively investigated as a model system for platelike colloids [37, 38, 39, 40, 41, 42, 43, 44, 45, 46, 47, 48, 49, 50, 51, 52, 53, 54, 55, 56, 57, 58, 59, 60, 61, 62, 63, 64, 65, 66, 67, 68, 69, 70, 71, 72, 73, 74, 75, 76, 77, 78, 79, 80]. A

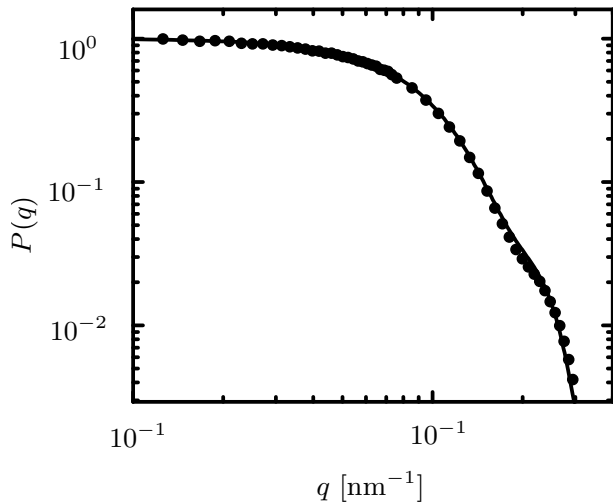


FIG. 3: The form factor  $P(q)$  of monodisperse stilbenoid dendrimers of the third generation [35] as obtained by small-angle neutron scattering (circles) and calculated according to Eq. (3).

theoretical description of such a well-characterized model clay appeared feasible. Early attempts focused on the structure of the electric double layer around a single platelet [40, 43, 44], or around two parallel platelets [50]. Much of the recent theoretical work was initiated by considering laponite platelets and their associated electric double layers as nonintersecting platelets carrying a constant electrostatic quadrupole moment [46]. The spatial arrangement of these objects has been investigated by Monte Carlo simulations. The results of these studies point to a reversible sol to gel transition at platelet number density  $\rho > 0.06 R^{-3}$ , where the structure of the gel phase is strongly reminiscent of a "house-of-cards".

A screened electrostatic potential between two arbitrary oriented, charged platelets has been worked out within the framework of a linearized Poisson-Boltzmann theory [45, 53, 61, 64]. At a fixed center-to-center distance, this repulsive electrostatic potential is maximized for coplanar platelets, which corresponds to the maximum overlap of electric double layers, and minimized when the platelets are coaxial and parallel. An intermediate potential is found for T-shaped perpendicular platelets. At present only preliminary results of Monte Carlo simulations for platelets interacting through such an anisotropic potential are available, indicating that the platelet fluid is in the isotropic phase for platelet number density  $\rho < 0.1 R^{-3}$  [61]. Later an interaction site model of laponite was put forward, and investigated by molecular-dynamics simulations [54] and integral equations [57]. In this model each platelet carries discrete charged sites rigidly arranged on an array inscribed in the platelet. Sites on different platelets interact via a repulsive screened Coulomb interaction. Upon varying the platelet number density and screening length, a sol, gel,

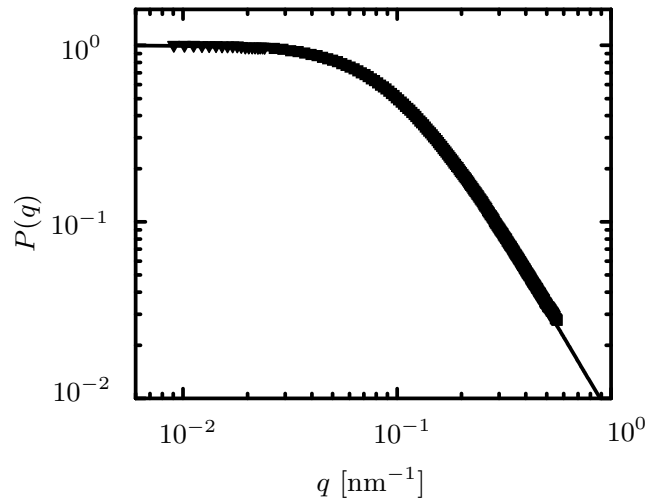


FIG. 4: The form factor  $P(q)$  of polydisperse laponite platelets [85] as obtained by light scattering (triangles) and small-angle x-ray scattering (squares). The solid line represents the theoretical results for polydisperse circular platelets according to Eqs. (2) - (4).

and crystal phase have been identified. Additional rim charges of opposite sign have been found to lead to T-shaped pair configurations and clustering of the platelets.

The theoretical studies on gelation and structure formation in laponite suspensions have assumed a system of monodisperse platelets, i.e., thin platelets with a radius  $R$  and a thickness  $L$ . However, it has become possible to visualize directly the laponite platelets by various techniques such as atomic force microscopy or electron microscopy. From these micrographs it is obvious that laponite exhibits a considerable size polydispersity [81, 82, 83, 84]. The degree of polydispersity has been quantified in a comprehensive study of laponite suspensions in dilute solution using light scattering and small-angle x-ray scattering [85]. Figure 4 displays the measured and calculated form factor  $P(q)$  of laponite platelets. From a comparison of Fig. 3 and Fig. 4 it is obvious that size polydispersity must be included in the case of laponite platelets because the form factor of monodisperse platelets given by Eq. (3) has a wavy shape which is smoothed out by size polydispersity in the case of the laponite platelets. The solid line in Fig. 4 shows the resulting fit obtained for a Schulz-Zimm-distribution with a polydispersity expressed through  $R_w/R_n = 1.6$ . The weight-average radius  $R_w$  is given by 11.5 nm, the thickness is found to be  $L=0.9$  nm, and the number-average radius is denoted by  $R_n$ . It is worthwhile to reiterate that laponite platelets exhibit an appreciable polydispersity that can be deduced from this analysis. Obviously, this must be taken into account when modeling the interaction of the particles at finite volume fraction.

### III. INTERMOLECULAR PAIR CORRELATIONS IN THE ISOTROPIC PHASE

Using the form factor as input into generalized Ornstein-Zernike equations of an interaction site integral equation theory, one can calculate structural properties of interacting platelets. In this section we will focus on results obtained from intermolecular pair correlation functions in the isotropic phase. Calculated structure factors will be compared with experimental data.

#### A. RISM and PRISM theory

The systems under investigation are dispersions or solutions, but in view of the mesoscopic scale of the particles, the solvent will be considered as a structureless continuum. Spatial pair correlations of an isotropic fluid of identical particles, each carrying  $n$  distinct interaction sites, are characterized by a set of intermolecular site-site total correlation functions  $h_{ij}(r, \rho)$ , where the indices  $i$  and  $j$  run over sites on each of two particles, and  $\rho$  is the particle number density. These functions are related to a set of intermolecular site-site direct correlation functions  $c_{ij}(r, \rho)$  by the generalized Ornstein-Zernike relations of the "reference interaction site model" (RISM), which in Fourier space read [86, 87]

$$h_{ij}(q, \rho) = \sum_{m,o=1}^n \omega_{im}(q) c_{mo}(q, \rho) (\omega_{oj}(q) + \rho h_{oj}(q, \rho)), \quad (5)$$

where the  $\omega_{ij}(q)$  are the Fourier transforms of the intramolecular correlation functions for rigid particles. For flexible particles the intramolecular correlation functions depend on the particle number density and follow from a statistical average over particle configurations. In the case of rigid particles such as the platelets considered here, the  $\omega_{ij}(q)$  are independent of the particle number density because the particles are not deformed due to intermolecular interactions for typical concentrations in the fluid state. The set of generalized Ornstein-Zernike equations must be supplemented by a set of closure relations. If the interaction sites are simply the centers of exclusion spheres of diameter  $d$ , to account for steric effects, a convenient closure is the Percus-Yevick approximation [86, 88]

$$h_{ij}(r, \rho) = -1, \quad r \leq d, \quad c_{ij}(r, \rho) = 0, \quad r > d. \quad (6)$$

The experimentally accessible structure factor  $S(q, \rho)$  is defined as

$$S(q, \rho) = 1 + \rho \frac{h(q, \rho)}{P(q)}, \quad (7)$$

where

$$h(q, \rho) = \frac{1}{n^2} \sum_{m,o=1}^n h_{mo}(q, \rho) \quad (8)$$

is the particle-averaged total correlation function. The particle-averaged intramolecular correlation function

$$P(q) = \frac{1}{n^2} \sum_{m,o=1}^n \omega_{mo}(q) \quad (9)$$

characterizes the geometry of the distribution of the sites, and hence the geometric shape of the particles. While the particle-averaged intramolecular correlation function accounts for the interference of radiation scattered from different parts of the same particle in a scattering experiment, the local order in the fluid is characterized by  $h(q, \rho)$  or  $S(q, \rho)$ .

The RISM has been proved to be a successful theory of the pair structure of many molecular fluids (for a review see Ref. [89]). In the case of macromolecular and colloidal systems, with very large numbers of interaction sites, the number of coupled RISM equations becomes intractable, and a considerable simplification follows from the assumption that the direct correlation functions  $c_{ij}(q, \rho)$  are independent of the indices  $i$  and  $j$ . This leads to the "polymer reference interaction site model" (PRISM) theory first applied by Schweizer and Curro to long flexible polymers [90]. PRISM neglects end effects in that case. The resulting single generalized Ornstein-Zernike equation of the PRISM reads

$$h(q, \rho) = P(q)c(q, \rho)P(q) + \rho c(q, \rho)h(q, \rho)P(q), \quad (10)$$

where  $c(q, \rho) = \sum_{m,o=1}^n c_{mo}(q, \rho)$ . Taking into account size polydispersity leads to coupled generalized Ornstein-Zernike equations of the multicomponent system consisting of  $N$  species:

$$h_{\alpha\gamma}(q, \{\rho_\alpha\}) = P_\alpha(q)c_{\alpha\gamma}(q, \{\rho_\alpha\})P_\gamma(q) + P_\alpha(q) \sum_{\delta=1}^N c_{\alpha\delta}(q, \{\rho_\alpha\})\rho_\delta h_{\delta\gamma}(q, \{\rho_\alpha\}). \quad (11)$$

This set of  $N(N+1)/2$  independent Ornstein-Zernike equations must be supplemented by as many closure relations between each pair of total and direct correlation functions. The PRISM integral equation theory has been successfully applied to various systems, such as rodlike viruses [91, 92, 93, 94], polymers [95, 96], mixtures of spherical colloids and semiflexible polymers [97], bottle-brush polymers [98], and polyelectrolyte brushes [99]. Moreover, it has been demonstrated that the simpler PRISM theory yields results in good agreement with the more elaborate RISM calculations for lamellar colloids [100].

#### B. Structure factor of stilbenoid dendrimers

In Fig. 5 the experimental structure factors  $S(q, \rho)$  for monodisperse stilbenoid dendrimers of the third generation (see Fig. 2) are compared to the results of the

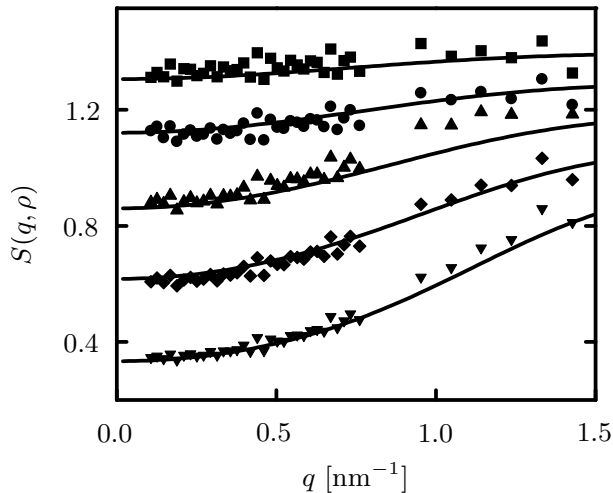


FIG. 5: Experimentally determined structure factors  $S(q, \rho)$  for monodisperse stilbenoid dendrimers of the third generation (see Fig. 2) together with the results of the theoretical predictions of the PRISM integral equation theory according to Eqs. (3), (7), and (10) [36]. The volume fraction of the dendrimers increases from top to bottom:  $\phi = 0.009, 0.019, 0.039, 0.061, 0.1$ . For reasons of clarity, the upper data sets and lines have been shifted up by 0.1, 0.2, 0.3, 0.4, respectively.

integral equation theory for the PRISM [36]. The calculated form factor  $P(q)$  (see the solid line in Fig. 3) has been used as input into the generalized Ornstein-Zernike equation [Eq. (10)]. The volume fraction is given by  $\phi = V_p \rho$ , where  $V_p$  is the volume of an individual particle. The generalized Ornstein-Zernike equation has been solved numerically together with the Percus-Yevick closure. From Fig. 5 it is apparent that the PRISM integral equation theory is rather accurate. The magnitude and the scattering vector range of the suppression of  $S(q, \rho)$ , i.e., the deviations from the value 1 at small scattering vectors, are characteristic for the size and the shape of the dendrimers as well as the volume fraction. On the basis of the experience with both PRISM and RISM it is expected that the results of the integral equation theory for the RISM would lead to very similar results, provided the same form factor is used [100].

### C. Scattering intensity of polyethylene nanoparticles

The above mentioned dispersions consisting of polydisperse polyethylene nanoplatelets (see Fig. 1) contained in addition just enough of the surfactant sodium dodecyl sulfate to stabilize the particles against coagulation [1]. The surface tension of 65 mN/m of the aqueous dispersion demonstrated that virtually all the surfactant was adsorbed onto the particles leading to an effective charge of the platelets which has to be taken into account in

the PRISM integral equation theory. One may consider a multicomponent system involving  $N$  species of charged platelets with number densities  $\rho_\alpha$ , where  $1 \leq \alpha \leq N$ . Each platelet of species  $\alpha$  contains  $n_\alpha$  equivalent interaction sites. The interaction potential between sites on particles of species  $\alpha$  and  $\gamma$ , carrying the charges  $z_\alpha e$  and  $z_\gamma e$ , is of the generic form:

$$U_{\alpha\gamma}(r) = \frac{z_\alpha z_\gamma e^2}{\epsilon r} \exp(-\kappa_D r), \quad (12)$$

where  $\lambda_D = \kappa_D^{-1}$  is the usual Debye screening length. The system is an aqueous dispersion, but in view of the mesoscopic scale of the platelets, the solvent is modelled as a structureless dielectric continuum providing a macroscopic permittivity  $\epsilon$ . Any microscopic counterions or ions from added electrolyte will be considered at the linear response (or Debye-Hückel) level, i.e., they will screen the electrostatic potential due to the interaction sites on the charged platelets on a scale given by the Debye screening length. The underlying assumption entails that the charge distribution on the mesoscopic particles does not contribute to screening.

The Laria-Wu-Chandler closure relation [101] has been used in order to supplement the Ornstein-Zernike equations [Eq. (11)] of the multicomponent system:

$$h_{\alpha\gamma}(r, \{\rho_\alpha\}) = \ln[h_{\alpha\gamma}(r, \{\rho_\alpha\}) + 1] + P_\alpha \star [c_{\alpha\gamma} + (k_B T)^{-1} n_\alpha n_\gamma U_{\alpha\gamma}] \star P_\gamma(r), \quad (13)$$

where the asterisk  $\star$  denotes a convolution product. In addition, steric effects have been taken into account using the Percus-Yevick approximation. The cryo-TEM micrograph displayed in Fig. 1 shows that the particles are hexagonal platelets with a pseudo-radius of 12.5 nm and a thickness of 6.3 nm. As argued above, however, the cryo-TEM micrograph shows only the crystalline lamella. Since polyethylene is a semicrystalline polymer, an amorphous layer in which the chains fold back must exist on both sides of the lamella. Hence, there must be a thin amorphous layer on both sides of the particles that needs to be taken into account. The form factor of such a "hamburger" is given by

$$P(q) = 4 \int_0^1 dx \frac{J_1^2(qR\sqrt{1-x^2})}{(qR\sqrt{1-x^2})^2} \left( L \frac{\sin(qLx/2)}{(qLx/2)} \Delta\tilde{\rho}_1 + L_c \frac{\sin(qL_c x/2)}{(qL_c x/2)} (\Delta\tilde{\rho}_c - \Delta\tilde{\rho}_1) \right)^2 \times (L\Delta\tilde{\rho}_1 + L_c(\Delta\tilde{\rho}_c - \Delta\tilde{\rho}_1))^{-2}. \quad (14)$$

Here  $R$  denotes the radius of the platelet,  $L$  is the overall thickness of the particles, while  $L_c$  denotes the thickness of the crystalline lamella.  $\Delta\tilde{\rho}_1$  and  $\Delta\tilde{\rho}_c$  are the contrasts of the outer two platelets and of the inner platelet, respectively. The polydispersity of the particles estimated from the cryo-TEM micrographs has been taken into account

in the fitting using a Gaussian distribution in radius and thickness. The closed set of equations (11) - (14) has been solved numerically by a standard iterative procedure in order to obtain the scattering intensity [1]. The solid lines in Fig. 6 display the form factors. The small-angle x-ray scattering intensities of the polyethylene nanoplatelets have been measured at six different contrasts starting from a stock solution of  $\phi = 0.017$  of the nanoplatelets dispersed in pure water. The different contrasts have been adjusted by adding different amounts of sucrose. The volume fractions of added sucrose increased from 0.0 (lowest contrast) to 0.378 (highest contrast) while the corresponding volume fraction of the nanoparticles decreased from  $\phi = 0.017$  to  $\phi = 0.007$ . For the sake of clarity the scattering intensities related to different contrast have been shifted vertically in Fig. 6. The figure demonstrates that varying the contrast leads to marked differences in the scattering intensities. In particular, the maxima of the scattering intensities are shifted in a characteristic manner when changing the contrast. The overall dimensions following from the theoretical description are the weight-average radius  $R_w = 12$  nm and the weight-average thickness  $L_w = 9$  nm. The thickness of the crystalline layer is  $L_c = 6.3$  nm. From the particle volume, the polyethylene density and the chain molecular weight, one can estimate that each particle is made up of ca. 14 chains. Moreover, from the entire series of small-angle x-ray scattering-intensities the contrast results to  $\Delta\tilde{\rho}_1 = 309$  electrons/nm<sup>3</sup> for the amorphous part and  $\Delta\tilde{\rho}_1 = 333$  electrons/nm<sup>3</sup> for the crystalline part. The electron densities of the crystalline and amorphous parts of the particles can be used to understand the cryo-TEM micrograph in detail. The value for  $\Delta\tilde{\rho}_1$  is close to the electron density of low density amorphous-ice. Therefore one can conclude that the amorphous parts are virtually matched in the cryo-TEM.

For small magnitudes of the scattering vector  $q$  the calculated scattering intensities for noninteracting particles (solid lines) on the one hand, and the integral equation results for interacting particles (dotted lines) as well as the experimental data (symbols) on the other hand deviate due to strong repulsive interactions between the particles. The observed decrease of the scattering intensity at small scattering vectors is considerably more pronounced than for fluids consisting of hard platelets such as the rigid dendrimers discussed above. From this result one can conclude that the colloidal stability is achieved by electrostatic repulsion between the platelets brought about by the adsorbed surfactant. It has been estimated that each polyethylene nanoplatelet is surrounded by a layer consisting of a few hundred surfactant molecules [1].

#### D. Structure factor of laponite

While the preceding subsections have demonstrated that the PRISM theory can describe pair correlations of both uncharged and uniformly charged platelike parti-

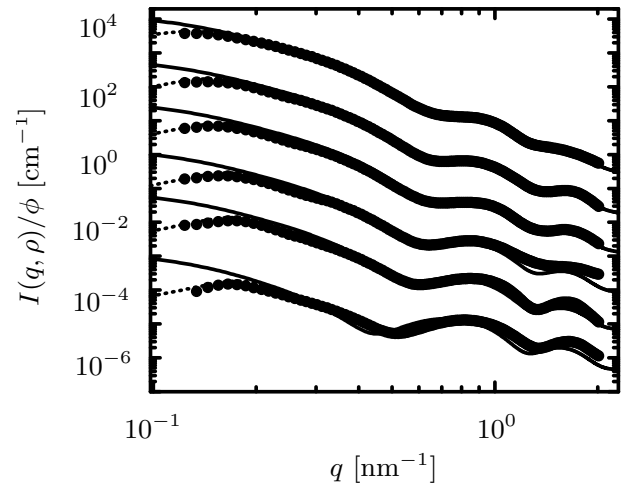


FIG. 6: Measured scattering intensity of polyethylene nanoplatelets as a function of the magnitude of the scattering vector  $q$  (symbols) [1]. All intensities have been normalized to the volume fraction  $\phi$  of the platelets in the dispersion. The volume fraction of the added sucrose increases from bottom to top (0, 6.2, 10.3, 18.0, 25.4, 37.8 vol.%) while the volume fraction  $\phi$  of the nanoplatelets decreases from bottom to top (1.73, 1.56, 1.44, 1.23, 1.02, 0.68 vol.%). The five lowest most intensities are shifted down by a factor of  $10^0$ ,  $10^2$ ,  $10^3$ ,  $10^4$ ,  $10^5$ , respectively. The solid lines represent the result of the modeling of the small-angle x-ray scattering data assuming a dispersion of noninteracting polydisperse platelets. The short dashed lines ( $q < 0.25$  nm<sup>-1</sup>) represent the scattering intensity calculated for a dispersion of interacting platelets as obtained from the PRISM integral equation theory [Eqs. (11) - (14)]. The differences between the dotted and solid lines reflect the intermolecular interaction between the nanoplatelets.

cles in solution, disagreement between experimental and theoretical results has been found in the case of laponite platelets if a purely repulsive screened Coulomb potential is used in the theoretical calculations [85]. It has been suggested [102] that at low concentrations the effective interaction between laponite platelets is characterized by a competition of long-range Coulomb repulsion and short-range van der Waals attraction similar to colloidal systems and protein solutions [103, 104, 105]. Moreover, the charge density is higher on the face than on the rim of a platelet, which leads to a modification of the interaction potential between sites on particles within the computationally demanding multicomponent PRISM theory. Therefore, a mesoscopic coarse graining, whereby particles act via an effective potential  $U(r)$  has been proposed [85]. To this end the Ornstein-Zernike equation

$$h(q, \rho) = c(q, \rho) + \rho c(q)h(q, \rho) \quad (15)$$

has been solved together with the hypernetted-chain closure relation

$$h(r, \rho) = \ln[h(r, \rho) + 1] + c(r, \rho) + (k_B T)^{-1} U(r). \quad (16)$$

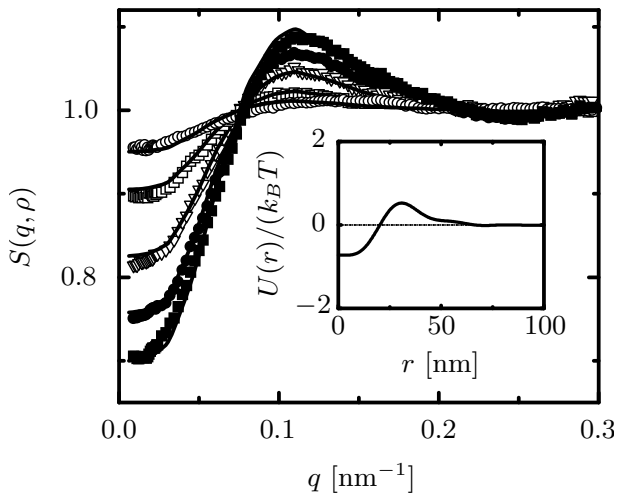


FIG. 7: The structure factor  $S(q, \rho)$  of laponite platelets for various volume fractions (open circles: 0.02 %; open squares: 0.04 %; open triangles: 0.08 %; solid circles: 0.12 %; solid squares: 0.16 %). The solid lines represent the results of the integral equation theory [Eqs. (15) - (17)] using the effective potential  $U(r)$  shown in the inset [85].

These equations follow from Eqs. (11) and (13) for  $N = 1$  and  $P_\alpha(q) = 1$ . The calculated structure factor

$$S(q, \rho) = 1 + \rho h(q, \rho) \quad (17)$$

is compared in Fig. 7 with experimental data [85]. For all volume fractions, good agreement with the experimental results has been achieved with a density-independent effective potential  $U(r)$  that is attractive for small distances but repulsive for larger distances (see the inset in Fig. 7). The effective potential fulfills the stability condition  $\int_0^\infty dr r^2 U(r) > 0$  discussed by Ruelle [106] and provides a representation of the underlying many-body interactions in the system. In general, to any  $S(q, \rho)$  there corresponds a unique effective center of mass potential  $U_{eff}(r, \rho)$ , capable of reproducing  $S(q, \rho)$ , irrespective of the underlying many-body interactions in the system. This effective potential is rather independent of the particle number density for the laponite suspensions, i.e.,  $U_{eff}(r, \rho) \approx U(r)$ .

Since structure factors and pair correlation functions of polyelectrolyte solutions calculated within the PRISM framework and using a purely repulsive screened Coulomb potential are in good agreement with experimental data and computer simulations, it is worthwhile to compare scattering data for polyelectrolytes with the data obtained for laponite. Figure 8 displays  $S(q = 0, \rho)$  together with  $S(q = q_{max}, \rho)$  for various polyelectrolytes and laponite [85], where  $q_{max}$  is the absolute value of the scattering vector at the main peak. The structure factors of the polyelectrolytes exhibit a main peak  $S(q = q_{max}, \rho) > 1$  and a small value  $S(q = 0, \rho) < 0.11$  for small scattering vectors, while the structure factors of laponite are characterized by a main peak and a rather

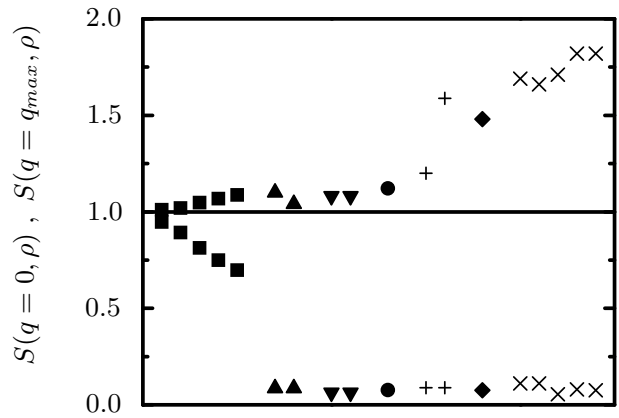


FIG. 8: The structure factor at zero scattering vector  $S(q = 0, \rho)$  (lower symbols) together with the structure factor at the main peak  $S(q = q_{max}, \rho)$  (upper symbols) for various suspensions: laponite at five volume fractions: 0.02 %, 0.04 %, 0.08 %, 0.12 %, 0.16 % from left to right (squares [85]); polystyrenesulfonate of length  $L = 6.8$  nm at two concentrations: 0.1 mol/L and 0.2 mol/L from left to right (up triangles [107]); polystyrenesulfonate of length  $L = 40$  nm at two concentrations: 0.1 mol/L and 0.2 mol/L from left to right (down triangles [107]); DNA of length  $L = 57$  nm at 0.05 mol/L (circles [107]); proteoglycan at two different salt concentrations: 0.05 mM and 0 mM from left to right (plus-symbols [108]); DNA of length  $L = 380$  nm at 0.05 mol/L (diamonds [107]); tobacco mosaic virus at five concentrations: 0.11 mg/mL, 0.27 mg/mL, 0.43 mg/mL, 1.05 mg/mL, 2.07 mg/mL from left to right (crosses [109]).

large value  $0.7 < S(q = 0, \rho) < 0.95$  for small scattering vectors. The enhancement of the small angle ( $q \rightarrow 0$ ) value of  $S(q, \rho)$  of laponite as compared to the polyelectrolyte signals increased density fluctuations. Since the polyelectrolyte solutions remain liquid like even at higher concentrations opposite to the laponite suspensions, the observed qualitative different behavior of the structure factors of laponite may be considered as indicative of the sol to gel transition at higher concentrations. In addition the values of  $S(q = 0, \rho)$  for the liquid like laponite suspensions are smaller than 1 and decrease with increasing concentration in contrast to strong small  $q$  upturns which have been observed experimentally for clay suspensions in the gel phase, polyelectrolyte gels and mixtures, and low ionic strength polyelectrolyte solutions. These strong upturns signal strong concentration fluctuations indicative of aggregation, or spinodal instability reminiscent of the behavior observed in computer simulations and PRISM integral equation theory of mixtures of oppositely charged particles [97].



#### IV. EQUATION OF STATE AND ISOTHERMAL COMPRESSIBILITY IN THE ISOTROPIC PHASE

The structure factor provides a direct link with thermodynamics via the compressibility equation [88]

$$\lim_{q \rightarrow 0} S(q, \rho) = \rho k_B T \kappa_T(\rho), \quad (18)$$

where  $\kappa_T(\rho)$  is the isothermal compressibility. The osmotic pressure  $P(\rho)$  (equation of state) then follows from

$$\frac{P(\rho)}{k_B T} = \int_0^\rho d\rho' S^{-1}(q=0, \rho'). \quad (19)$$

Various attempts have been made to develop accurate theories for the equation of state of fluids consisting of nonspherical particles:

(a) Scaled particle theory, which is very successful for hard sphere fluids, has been extended to prolate and oblate ellipsoids of revolution [110], however with moderate success when gauged against Monte Carlo simulations [111]. Recently, it has been shown [112] that the results of scaled particle theory [112, 113, 114] for platelike particles or the closely related model of hard cut spheres are in disagreement with computer simulation data [14, 115, 116, 117, 118, 119, 120].

(b) Onsager theory [121, 122], based on the second virial coefficient alone, can be "rescaled" [123, 124, 125]. Although this semi-empirical procedure leads to reasonably good results for rodlike particles, it is much less satisfactory for platelike particles [126].

(c) Many theoretical studies on hard sphere fluids and depletion agents use the so-called free volume theory [127], in which the free volume accessible to a single particle plays a major role. This free volume theory has been studied within a fundamental measure theory [112]. However, it has been demonstrated that the resulting third virial coefficients of the equation of state for both hard cylinders and hard cut spheres differ from computer simulation results (see tables I and II in Ref. [112]). Theoretical approaches based on fundamental measure theory do not yield correct third virial coefficients and equation of states due to the occurrence of so-called lost cases, i.e., the fact that configurations of three particles with pairwise overlap but no triple overlap do not contribute to thermodynamic properties (see, e.g., Refs. [128, 129, 130]).

These theoretical and computer simulation studies demonstrate that the understanding of thermodynamic properties of nonspherical particles needs to be improved. Recently, the measured inverse structure factor  $S^{-1}(q=0, \rho)$  extrapolated to vanishing scattering vectors of stilbenoid dendrimers of the third generation has been modelled in terms of the so-called  $y3$  expansion [131, 132]

$$S^{-1}(q=0, \rho) = \frac{1 + 2(B_2 V_p - 2)\phi + (3B_3 V_p^2 - 8B_2 V_p + 6)\phi^2}{(1 - \phi)^4} \quad (20)$$

$$\approx 1 + 2B_2 \rho + 3B_3 \rho^2 + O(\rho^3). \quad (21)$$

The  $y3$  theory reproduces the exact second and third virial coefficients,  $B_2$  and  $B_3$ , respectively. However, its practical applicability is limited due to the difficult numerical evaluation of the third virial coefficient  $B_3$  in the case of nonspherical particles [133], while the second virial coefficient  $B_2$  for an isotropic hard convex body fluid is known exactly (see Ref. [134] and references therein):

$$B_2 = V_p + A_p \tilde{R}_p. \quad (22)$$

Here  $A_p$  and  $\tilde{R}_p = (1/4\pi) \int dA_p H_p$  are the surface area and the mean radius, respectively, where the local mean curvature is denoted as  $H_p$ . For a circular platelet of radius  $R$  and thickness  $L$  one has  $V_p = \pi R^2 L$ ,  $A_p = 2\pi R(R + L)$ , and  $\tilde{R}_p = \pi R/4 + L/4$ . For platelike stilbenoid dendrimers of the third generation the second virial coefficient  $B_2/V_p = 5.54$  as calculated from Eq. (22) with  $R = 2.4$  nm and  $L = 1.8$  nm agrees with the experimentally determined second virial coefficient [36].

In the framework of both scaled particle theory and Rosenfeld's fundamental measure theory  $S^{-1}(q=0, \rho)$  is also given by Eqs. (20) and (21) but the third virial coefficient reads

$$B_3^{(SPT)} = V_p^2 + 2\tilde{R}_p A_p V_p + \frac{1}{3} \tilde{R}_p^2 A_p^2 \quad (23)$$

within scaled particle theory and

$$B_3^{(FMT)} = V_p^2 + 2\tilde{R}_p A_p V_p + \frac{1}{12\pi} A_p^3 \quad (24)$$

within fundamental measure theory. In Fig. 9 the experimentally determined inverse structure factor  $S^{-1}(q=0, \rho)$  extrapolated to vanishing scattering vectors of stilbenoid dendrimers of the third generation is compared with the results of scaled particle theory according to Eqs. (20), (22), and (23) and fundamental measure theory according to Eqs. (20), (22), and (24). With increasing volume fraction the theoretical results of both scaled particle theory (dashed line) and fundamental measure theory (dotted line) deviate from the experimental data (symbols). These deviations are mainly due to the fact that the predicted third virial coefficients  $B_3^{(SPT)}$  and  $B_3^{(FMT)}$  are too small. However, the PRISM theory discussed above leads to an agreement with the experimental data as is apparent from Fig. 5 [36].

This comparison of experimentally determined  $S^{-1}(q=0, \rho)$  of platelike particles with the predictions of the well-known scaled particle and fundamental measure theory has confirmed earlier caveats concerning the applicability of these theories to freely rotating nonspherical particles [112]. For example,  $B_3^{(FMT)} = 2\pi^2 R^6/3 = 6.580R^6$  as calculated from Eq. (24) for thin circular platelets in the limit  $L \rightarrow 0$  underestimates the third virial coefficient  $B_3 = 10.829R^6$  according to computer simulation studies [116, 118].

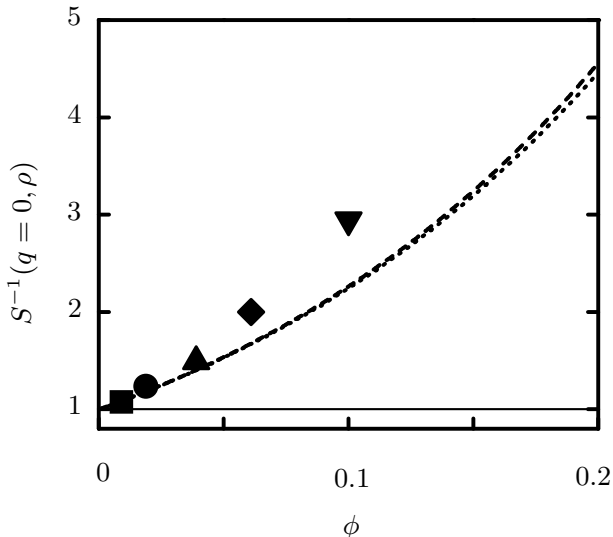


FIG. 9: Inverse structure factor  $S^{-1}(q = 0, \rho)$  extrapolated to vanishing scattering vectors of stilbenoid dendrimers of the third generation (with the same symbol code as in Fig. 5). The dashed line follows from the scaled particle theory according to Eqs. (20), (22), and (23) while the dotted line represents the results of the fundamental measure theory as obtained from Eqs. (20), (22), and (24) [36].

## V. ORIENTATIONAL ORDER IN SPATIALLY HOMOGENEOUS BULK PHASES

In this section we will outline some points on the basic description of orientational order in platelet dispersions and we will record details about the phase behavior of spatially homogeneous bulk fluids.

### A. Density functional theory

The systems under investigation are dispersions involving  $N$  species of colloidal particles. The number density of the centers of mass of platelets of species  $i$  at a point  $\mathbf{r}$  with an orientation  $\boldsymbol{\omega} = (\theta, \phi)$  of the normal of the platelets (see Fig. 10) is denoted by  $\rho_i(\mathbf{r}, \boldsymbol{\omega})$  while for spherical structureless particles the center of mass number density is independent of  $\boldsymbol{\omega}$ . The equilibrium density profiles of the fluid under the influence of external potentials  $U_i(\mathbf{r}, \boldsymbol{\omega})$  minimize the grand potential functional [134, 135, 136]

$$\begin{aligned} \Omega[\{\rho_i\}] &= F_{id}[\{\rho_i\}] + F_{ex}[\{\rho_i\}] \\ &+ \sum_{i=1}^N \int d^3r d\boldsymbol{\omega} \rho_i(\mathbf{r}, \boldsymbol{\omega}) (U_i(\mathbf{r}, \boldsymbol{\omega}) - \mu_i). \end{aligned} \quad (25)$$

Here  $\mu_i$  is the chemical potential of particles of species  $i$  and  $F_{id}[\{\rho_i\}] + F_{ex}[\{\rho_i\}]$  is the intrinsic Helmholtz free energy of the fluid (i.e., the Helmholtz free energy in the absence of the external potentials).  $F_{id}[\{\rho_i\}]$  is the

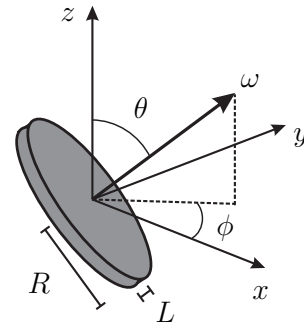


FIG. 10: Illustrations of the polar angle  $\theta$  and the azimuthal angle  $\phi$  of the normal  $\boldsymbol{\omega}$  of a platelet of radius  $R$  and thickness  $L$ . The center of mass of the particle is located at  $\mathbf{r} = (0, 0, 0)$ .

intrinsic Helmholtz free energy of an ideal gas of noninteracting particles,

$$\begin{aligned} F_{id}[\{\rho_i\}] &= k_B T \sum_{i=1}^N \int d^3r d\boldsymbol{\omega} \rho_i(\mathbf{r}, \boldsymbol{\omega}) \\ &\times (\ln[4\pi\Lambda_i^3 \rho_i(\mathbf{r}, \boldsymbol{\omega})] - 1), \end{aligned} \quad (26)$$

where  $\Lambda_i$  is the corresponding thermal de Broglie wavelength. The excess (over the ideal gas) free energy functional  $F_{ex}[\{\rho_i\}]$  is in general a very complicated, highly non-trivial object, because it is a characteristic property of an interacting many-body system. The functional  $F_{ex}[\{\rho_i\}]$  is dealt with in various ways, which specify the explicit forms of the theory.

By means of a diagrammatic expansion it can be shown that the exact excess free energy functional in the low density limit reduces to a virial approximation, which is the starting point of the following considerations. Within a third-order virial approximation the excess free energy functional is given by

$$\begin{aligned} F_{ex}[\{\rho_i\}] &= \\ &- \frac{k_B T}{2} \sum_{i,j=1}^N \int d^3r_1 d^3r_2 d\boldsymbol{\omega}_1 d\boldsymbol{\omega}_2 \rho_i(\mathbf{r}_1, \boldsymbol{\omega}_1) \\ &\times f_{ij}(\mathbf{r}_1, \boldsymbol{\omega}_1; \mathbf{r}_2, \boldsymbol{\omega}_2) \rho_j(\mathbf{r}_2, \boldsymbol{\omega}_2) \\ &\times (1 + \frac{1}{3} \sum_{k=1}^N \int d^3r_3 d\boldsymbol{\omega}_3 f_{jk}(\mathbf{r}_2, \boldsymbol{\omega}_2; \mathbf{r}_3, \boldsymbol{\omega}_3) \\ &\times \rho_k(\mathbf{r}_3, \boldsymbol{\omega}_3) f_{ki}(\mathbf{r}_3, \boldsymbol{\omega}_3; \mathbf{r}_1, \boldsymbol{\omega}_1)), \end{aligned} \quad (27)$$

where  $f_{ij}(\mathbf{r}_1, \boldsymbol{\omega}_1; \mathbf{r}_2, \boldsymbol{\omega}_2)$  is the Mayer function of the pair interaction potential between two particles of species  $i$  and  $j$ . For sterically stabilized colloidal particles the most important feature of their pair interaction is the strong mutual repulsion whenever the distance between the centers of mass of the particles is smaller than that at which their surfaces touch each other. For nonspherical particles this shape-dependent repulsion is a function of the mutual orientation of the particles. In view of the

steepness of the repulsive potential between two particles, the latter may be regarded as hard particles, such that the pair interaction potential is infinite if the particle volumes overlap and is zero otherwise. By matching the indices of refraction of the colloidal particles and the solvent it is possible to effectively switch off the omnipresent dispersion forces and to create colloidal suspensions in which the actual effective interaction between the colloidal particles very closely resembles this hard core potential. In this way theoretical models of hard body fluids have their actual experimental counterparts with which their properties can be compared quantitatively. For such hard body fluids the corresponding Mayer function equals  $-1$  if the hard particles overlap and is zero otherwise [88]. Two thin platelets ( $R \gg L$ , see Fig. 10), separated by a distance  $\mathbf{r}_{12}$ , intersect if the inequality

$$|\mathbf{r}_{12} \cdot (\boldsymbol{\omega}_1 \times \boldsymbol{\omega}_2)| < \sqrt{R^2 \sin^2 \gamma_{12} - (\mathbf{r}_{12} \cdot \boldsymbol{\omega}_1)^2} + \sqrt{R^2 \sin^2 \gamma_{12} - (\mathbf{r}_{12} \cdot \boldsymbol{\omega}_2)^2} \quad (28)$$

with  $\boldsymbol{\omega}_j = (\sin \theta_j \cos \phi_j, \sin \theta_j \sin \phi_j, \cos \theta_j)$ ,  $j = 1, 2$ , and  $\mathbf{r}_{12} = \mathbf{r}_1 - \mathbf{r}_2$  is fulfilled [116].  $\gamma_{12}$  is the angle between the normals  $\boldsymbol{\omega}_1$  and  $\boldsymbol{\omega}_2$  of the two platelets. For thin platelets the intersection volume is like a line segment for  $\boldsymbol{\omega}_1 \neq \boldsymbol{\omega}_2$ . Configurations with exactly equal orientations  $\boldsymbol{\omega}_1 = \boldsymbol{\omega}_2$  are not considered for freely rotating thin platelets in three dimensions because they have a vanishing statistical weight. Minimization of  $\Omega$  with respect to  $\rho_i(\mathbf{r}, \boldsymbol{\omega})$  leads to integral equations for the equilibrium density profiles:

$$\rho_i(\mathbf{r}, \boldsymbol{\omega}) = \frac{1}{4\pi\Lambda_i^3} \exp\left(-\frac{1}{k_B T} \frac{\partial F[\{\rho_i\}]}{\partial \rho_i(\mathbf{r}, \boldsymbol{\omega})}\right). \quad (29)$$

These equations can be solved numerically for given chemical potentials  $\mu_i$  and given external potentials  $U_i(\mathbf{r}, \boldsymbol{\omega})$  using a Picard scheme with retardation, i.e., the equations  $\rho_i(\mathbf{r}, \boldsymbol{\omega}) = J[\{\rho_i\}]$  are solved according to  $\rho_i^{(l)}(\mathbf{r}, \boldsymbol{\omega}) = \text{mix} J[\{\rho_i^{(l-1)}\}] + (1 - \text{mix})\rho_i^{(l-1)}(\mathbf{r}, \boldsymbol{\omega})$  with a mixing parameter  $0 < \text{mix} < 1$ . Starting from an initial guess for  $\rho_i^{(0)}(\mathbf{r}, \boldsymbol{\omega})$ , the solutions of the equations are obtained by an iterative approach  $l = 0, 1, 2, \dots$ . The mixing parameter is adjusted empirically to ensure convergence. In practice, first the Mayer functions are calculated and are stored for all required values of  $(\mathbf{r}_1, \boldsymbol{\omega}_1; \mathbf{r}_2, \boldsymbol{\omega}_2)$ . Thereafter the integral equations [Eq. (29)] are solved.

For a homogeneous and isotropic bulk fluid with  $U_i(\mathbf{r}, \boldsymbol{\omega}) = 0$  in a macroscopic volume  $V$  the grand potential functional [Eq. (25)] reduces to

$$\frac{\Omega_b}{Vk_B T} = \sum_{i=1}^N \rho_i (\ln(\Lambda_i^3 \rho_i) - 1 - \mu_i (k_B T)^{-1}) + \sum_{i,j=1}^N \rho_i \rho_j \left( B_2^{(ij)} + \frac{1}{2} \sum_{k=1}^N B_3^{(ijk)} \rho_k \right), \quad (30)$$

where  $\rho_i = V^{-1} \int d^3 r d\boldsymbol{\omega} \rho_i(\mathbf{r}, \boldsymbol{\omega})$  are the total particle number densities.  $B_2^{(ij)}$  is the second virial coefficient between particles of species  $i$  and  $j$ :

$$B_2^{(ij)} = -\frac{1}{2(4\pi)^2} \int d^3 r_1 d\boldsymbol{\omega}_1 d\boldsymbol{\omega}_2 f_{ij}(\mathbf{r}_1, \boldsymbol{\omega}_1; 0, \boldsymbol{\omega}_2). \quad (31)$$

In accordance with the standard definition [88], the third virial coefficient involving three particles of species  $i, j, k$  is given by

$$B_3^{(ijk)} = -\frac{1}{3(4\pi)^3} \int d^3 r_1 d^3 r_2 d\boldsymbol{\omega}_1 d\boldsymbol{\omega}_2 d\boldsymbol{\omega}_3 \times f_{ij}(\mathbf{r}_1, \boldsymbol{\omega}_1; 0, \boldsymbol{\omega}_2) f_{jk}(\mathbf{r}_1 - \mathbf{r}_2, \boldsymbol{\omega}_2; 0, \boldsymbol{\omega}_3) \times f_{ki}(\mathbf{r}_2, \boldsymbol{\omega}_3; 0, \boldsymbol{\omega}_1). \quad (32)$$

The equation of state derived from the grand potential [Eq. (30)] takes the following form:

$$\frac{P}{k_B T} = -\frac{1}{k_B T} \left( \frac{\partial \Omega_b}{\partial V} \right)_{T, \{\mu_i\}} \quad (33)$$

$$= \left( \sum_{i=1}^N \rho_i + \sum_{i,j=1}^N B_{ij}^{(2)} \rho_i \rho_j + \sum_{i,j,k=1}^N B_{ijk}^{(3)} \rho_i \rho_j \rho_k \right). \quad (34)$$

The same equation without the second and the third term on the right-hand side holds for the ideal gas limit, i.e., noninteracting particles.

## B. Fundamental measure theory for thin hard platelets in three dimensions

Within a geometry-based density functional theory the excess free energy functional for monodisperse thin platelets in three dimensions is obtained by integrating over an excess free energy density,

$$F_{ex}[\rho] = \frac{k_B T}{16\pi^2} \int d^3 r d\boldsymbol{\omega}_1 d\boldsymbol{\omega}_2 \Phi(\{n_\nu\}), \quad (35)$$

where the spatial and angular arguments of the weighted densities  $n_\nu$  are suppressed in the notation. The free energy density  $\Phi$  is given by [137]

$$\Phi(\{n_\nu\}) = n_1(\mathbf{r}, \boldsymbol{\omega}_1) n_2(\mathbf{r}, \boldsymbol{\omega}_1) + \frac{1}{24\pi} n_2(\mathbf{r}, \boldsymbol{\omega}_1) n_3(\mathbf{r}, \boldsymbol{\omega}_1; \boldsymbol{\omega}_2) n_2(\mathbf{r}, \boldsymbol{\omega}_2). \quad (36)$$

The weighted densities are related to the number density of the center of mass of the platelets  $\rho(\mathbf{r}, \boldsymbol{\omega})$  according to

$$n_1(\mathbf{r}, \boldsymbol{\omega}_1) = \int \frac{d\boldsymbol{\omega}'}{4\pi} w_1(\mathbf{r}, \boldsymbol{\omega}'; \boldsymbol{\omega}_1) \star \rho(\mathbf{r}, \boldsymbol{\omega}'), \quad (37)$$

$$n_2(\mathbf{r}, \boldsymbol{\omega}_1) = w_2(\mathbf{r}, \boldsymbol{\omega}_1) \star \rho(\mathbf{r}, \boldsymbol{\omega}_1), \quad (38)$$

$$n_3(\mathbf{r}, \boldsymbol{\omega}_1; \boldsymbol{\omega}_2) = \int \frac{d\boldsymbol{\omega}'}{4\pi} w_3(\mathbf{r}, \boldsymbol{\omega}'; \boldsymbol{\omega}_1; \boldsymbol{\omega}_2) \star \rho(\mathbf{r}, \boldsymbol{\omega}'), \quad (39)$$

where the asterisk  $\star$  denotes the spatial convolution and the weight functions are given by

$$w_0(\mathbf{r}, \boldsymbol{\omega}_1) = \frac{1}{8} \delta(R - |\mathbf{r}|) \delta(\mathbf{r} \cdot \boldsymbol{\omega}_1), \quad (40)$$

$$w_2(\mathbf{r}, \boldsymbol{\omega}_1) = 2\Theta(R - |\mathbf{r}|) \delta(\mathbf{r} \cdot \boldsymbol{\omega}_1), \quad (41)$$

$$w_1(\mathbf{r}, \boldsymbol{\omega}_1; \boldsymbol{\omega}_2) = \frac{2}{R} |\boldsymbol{\omega}_1 \cdot (\boldsymbol{\omega}_2 \times \mathbf{r})| w_0(\mathbf{r}, \boldsymbol{\omega}_1), \quad (42)$$

$$w_3(\mathbf{r}, \boldsymbol{\omega}_1; \boldsymbol{\omega}_2; \boldsymbol{\omega}_3) = \frac{8}{\pi} |\boldsymbol{\omega}_1 \cdot (\boldsymbol{\omega}_2 \times \boldsymbol{\omega}_3)| w_2(\mathbf{r}, \boldsymbol{\omega}_1). \quad (43)$$

Here  $\Theta(x)$  is the Heaviside step function and  $\delta(x)$  is the Dirac distribution. The Mayer function of the pair interaction potential between two hard platelets [Eq. (28)] is recovered via the convolution

$$f(\mathbf{r}, \boldsymbol{\omega}_1; 0, \boldsymbol{\omega}_2) = -2w_2(\mathbf{r}, \boldsymbol{\omega}_1) \star w_1(\mathbf{r}, \boldsymbol{\omega}_1; \boldsymbol{\omega}_2). \quad (44)$$

However, the fundamental measure theory does not yield the correct third virial coefficient due to the above mentioned occurrence of lost cases [137]. The fundamental measure approximation for the third virial coefficient is nonvanishing only for three platelets at position vectors  $\mathbf{r}_1, \mathbf{r}_2, \mathbf{r}_3$  with a common triple intersection. The lost cases are compensated by overcounting the cases with triple intersections, such that the resulting equation of state is in reasonable agreement with the exact results for the isotropic bulk fluid. In the case of thin platelets this has been achieved by using the prefactor  $1/(24\pi)$  in the second term in Eq. (36) which leads to the third virial coefficient  $B_3^{(FMT)} = 2\pi^2 R^6/3$ . The equation of state as obtained from this fundamental measure theory is indeed in reasonable agreement with computer simulation data as is apparent from Fig. 11.

The density functional theory allows one to consider the possibility of an isotropic to nematic phase transition in a monodisperse fluid of platelets as a function of particle number density. The broken symmetry in the spatially homogeneous nematic phase may be characterized by the nematic order parameter

$$S = \frac{1}{8\pi\rho V} \int d^3r d\boldsymbol{\omega} \rho(\mathbf{r}, \boldsymbol{\omega}) (3 \cos^2 \theta - 1) \quad (45)$$

which varies between 0 in the isotropic phase and 1 when all platelets are oriented along one axis. For the bulk isotropic (I) to nematic (N) phase transition the following values of the particle number density and the nematic order parameter at two-phase coexistence have been obtained from fundamental measure theory:  $\rho_I R^3 = 0.42$ ,  $\rho_N R^3 = 0.46$ ,  $S_I = 0.05$ , and  $S_N = 0.49$  [137]. These values are similar to the ones obtained from computer simulations while a second virial approximation based on Eq. (27) without the last term overestimates both the density jump and the nematic order parameter at coexistence and yields  $\rho_I R^3 = 0.67$ ,  $\rho_N R^3 = 0.85$ , and  $S_N = 0.79$ . Even for thin platelets the chance that one platelet has contact with two or more platelets simultaneously is significant, and thus for this fluid the third virial

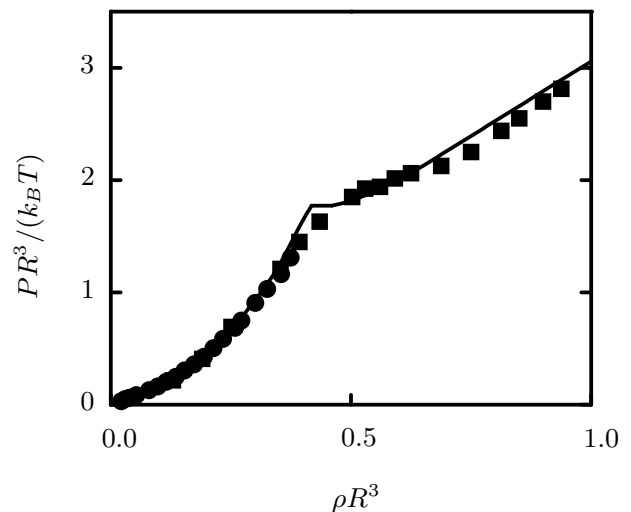


FIG. 11: Equation of state of thin platelets ( $R \gg L$ , see Fig. 10) as obtained from fundamental measure theory according to Eqs. (35) - (43) (solid line [137]) and from computer simulations (circles [116] and squares [46]). The horizontal line is the tie-line illustrating isotropic-nematic two-phase coexistence according to the fundamental measure theory.

coefficient is non-negligible. For comparison we note that the contribution of the third virial coefficient to the equation of state of a fluid consisting of thin rods is vanishing small, reflecting the small probability that three rods will simultaneously intersect [122].

Density functional theory has been applied to fluids consisting of thin hard platelets in contact with a hard substrate [138]. Platelets lying very close to the substrate must adopt nearly a fully parallel alignment due to interactions with the substrate. The probability of finding platelets touching the substrate is increased compared with the bulk due to effective entropic interactions. Upon increasing the bulk platelet density the substrate is completely wetted by a nematic film [139]. For the fluid confined by two parallel hard substrates, a first-order capillary nematization transition for large slit widths has been determined [140].

The enrichment and ordering of clay platelets near surfaces is important for the oil and gas production [141]. The first stage of recovering oil and gas from an underground reservoir is the drilling of wells into the hydrocarbon-bearing rock. This is performed by rotary drilling using, for example, water-based drilling fluids that contain smectic clay platelets such as bentonite or montmorillonite. Among the many functions that drilling fluids must possess to be successful for a drilling operation are: carrying the drilling cuttings and transporting them back to the surface; suspending the drilled cuttings when circulation is stopped; cooling and cleaning the bit; reducing the friction between the drilling string and the sides of the hole; preventing the inflow of fluids from the permeable rocks that are penetrated;

maintaining the stability of the wellbore; and forming a thin, low permeability filter-cake which seals the pores and other openings in formations penetrated by the bit. Scanning electron microscope images of mixed-metal hydroxide - bentonite filter-cake formed on the surface of a sandstone rock show in detail how the mixed-metal hydroxide and bentonite platelets form bridges across the entrance of rock pores of size  $30 \mu\text{m}$  and larger, although the radius of an individual platelet is less than  $0.5 \mu\text{m}$  [141]. Effective entropic interactions together with van der Waals interactions at submicron distances play an important role in understanding the underlying mechanisms of orientational ordering near surfaces [142]. Density functional theory provides the basic description of such inhomogeneous colloidal platelet fluids [134].

### C. Strictly two-dimensional hard platelets

The density functional theory presented in the previous subsection is based on the weight functions given by Eqs. (40) - (43) and the deconvolution of the Mayer function [Eq. (44)]. Although the particle shape is equivalent, overlapping pair configurations are very different for freely rotating platelets in three dimension as compared to the strictly two-dimensional case. While for thin platelets in three dimensions the intersection volume is like a line segment ( $\omega_1 \neq \omega_2$ ), the intersection volume is an area for platelets in two dimensions ( $\omega_1 = \omega_2$ ). Rosenfeld's weight functions for two-dimensional hard platelets of radius  $R$  are [130, 143, 144, 145]

$$w_2(\mathbf{r}) = \Theta(R - |\mathbf{r}|), \quad (46)$$

$$w_1(\mathbf{r}) = \delta(R - |\mathbf{r}|), \quad (47)$$

$$\mathbf{w}_1(\mathbf{r}) = w_2(\mathbf{r}) \frac{\mathbf{r}}{|\mathbf{r}|}, \quad (48)$$

$$w_0(\mathbf{r}) = w_1(\mathbf{r}) \frac{1}{2\pi R}. \quad (49)$$

The exact Mayer function is approximated by

$$\tilde{f}(\mathbf{r}) = 2w_0(\mathbf{r}) \star w_2(\mathbf{r}) + \frac{1}{2\pi} (w_1(\mathbf{r}) \star w_1(\mathbf{r}) - \mathbf{w}_1(\mathbf{r}) \star \mathbf{w}_1(\mathbf{r})), \quad (50)$$

where  $\mathbf{r}$  is the center to center vector and the asterisk  $\star$  denotes the two-dimensional convolution. The evaluation of the integrals in Eq. (50) yields [137]

$$\tilde{f}(r) = \Theta(2R - r) \left( \frac{2}{\pi} \arccos\left(\frac{r}{2R}\right) + \frac{r}{\pi\sqrt{4R^2 - r^2}} \right). \quad (51)$$

Figure 12 illustrates that  $f(\mathbf{r})$  and  $\tilde{f}(\mathbf{r})$  differ qualitatively. In particular,  $\tilde{f}(\mathbf{r})$  exhibits a divergence in the case that the two platelets touch each other, i.e., for  $|\mathbf{r}| = 2R$ . However the deviations from the exact value (solid

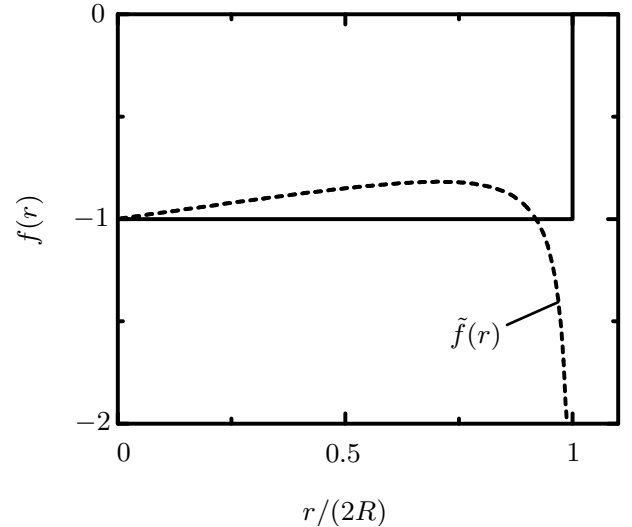


FIG. 12: The exact Mayer function  $f(r)$  for platelets of radius  $R$  in two dimensions (solid line) and the approximate representation  $\tilde{f}(r)$  according to the fundamental measure theory (dashed line) as obtained from Eq. (51), respectively. The distance between the centers of the platelets is denoted by  $r$ . Note that  $\tilde{f}(r)$  diverges upon approaching  $r = 2R$ .

line in Fig. 12) balance such that the second virial coefficient is exact, i.e.,  $\int d^2r f(\mathbf{r}) = \int d^2r \tilde{f}(\mathbf{r})$ . Higher order virial coefficients have been calculated recently using molecular dynamics simulations [146]. Moreover, the fundamental measure theory for two-dimensional platelets has been considered as a useful tool to study inhomogeneous systems such as laser induced freezing and melting of confined colloidal particles [147] despite the deficiencies of the theory in reproducing the Mayer function.

### D. Colloidal mixtures of hard spheres and platelets

Depletion interactions between large colloidal particles induced by smaller particles, which can be either solvent particles or a colloidal component in its own right, are of significant research interest because of the importance of these effective interactions in various colloidal processes. For example, flocculation of colloids can be driven by the addition of non-adsorbing polymers via the depletion mechanism. On the other hand, stabilization of colloidal suspensions can be achieved by the addition of adsorbing polymers. Whereas experimental and theoretical studies have focused on binary hard-sphere fluids as well as on colloidal mixtures of hard spheres and hard rods or polymers, less attention has been paid to hard platelets acting as depletants [112, 148, 149, 150, 151, 152, 153, 154].

Density functional theory for thin hard platelets has been used to investigate the depletion potential between two hard spheres due to the presence of thin platelets [150]. The calculated depletion potential between two

spheres exhibits an attractive primary minimum at contact when the spheres touch each other. This minimum deepens upon increasing the platelet density and a small repulsive barrier at larger sphere separations develops. However, the depletion barrier is typically less than the thermal energy  $k_B T$ , and therefore unlikely to significantly alter the kinetics of aggregation of the hard spheres at platelet densities smaller than one half the density of the isotropic phase at bulk isotropic-nematic two-phase coexistence. Nonetheless, with increasing platelet density the integrated strength of the effective interaction between the spheres becomes significantly weaker and thus reduces the thermodynamic onset of flocculation [150].

A fundamental measure-based density functional theory has been used to study binary colloidal fluids consisting of hard spheres and thin platelets in their bulk and near a planar hard substrate. Figure 13 displays the calculated phase diagram for a binary mixture of spheres and thin platelets for a size ratio  $R_S/R = 2$ , where  $R_s$  is the radius of the spheres [153]. The tie-lines are horizontal because the coexisting phases are characterized by the equality of the chemical potential of the platelets  $\mu$  in the coexisting phases. The binodal for coexisting states is shown, for which a sphere-rich and a platelet-poor liquid phase coexists with a sphere-poor and a platelet-rich liquid phase. The coexistence region is bounded by a lower critical point below which only a single stable phase is found. Upon decreasing  $\mu$  the adsorption behavior of the mixture near a planar substrate changes qualitatively so that two cases have to be distinguished. For  $\mu/(k_B T) > -5.551$  the sphere-rich phase does not wet the wall at two-phase coexistence. The layer thickness of the sphere-rich phase forming close to the wall increases continuously upon approaching the bulk phase boundary, but remains finite at coexistence. For  $\mu/(k_B T) < -5.551$ , however, the wall is wetted completely. The transition to complete wetting is first-order because the excess adsorptions of both the spheres and platelets along the bulk coexistence curve jump to macroscopic values upon crossing the wetting transition point.

Binary mixtures of silica spheres of radius  $R_s = 350$  nm and silica-coated gibbsite platelets of radius  $R = 229$  nm and thickness  $L = 56$  nm have been investigated by means of confocal microscopy and TEM [154]. The depletion-induced aggregation of the spherical particles has been observed in a TEM micrograph. In contrast to sphere-polymer and sphere-rod mixtures, the addition of platelets to a solution of spheres close to the fluid-solid binodal of the latter slowed down early crystalline ordering of the spheres, which led to more grain boundaries and powder-like structures. It has been argued that in the two-phase region the disordered sediment structures are kinetically arrested, which prevents further crystallization. Moreover, fluid-like microphases of platelets were trapped in the sediment which is due to the simultaneous sedimentation of platelets and spheres

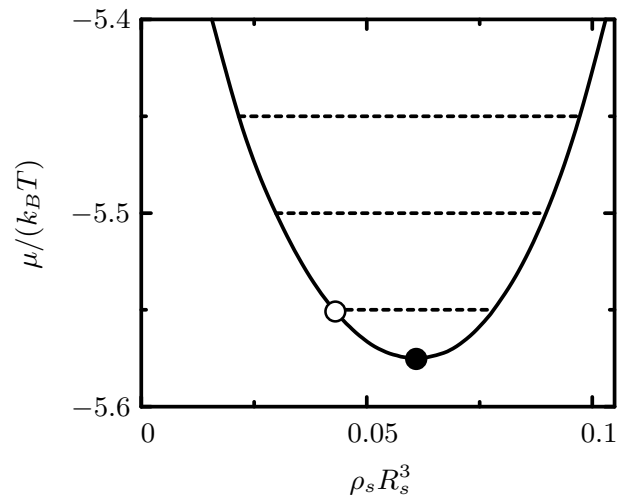


FIG. 13: Bulk and surface phase diagrams of binary mixtures of spheres of radius  $R_s$  and thin platelets of radius  $R = R_s/2$  as a function of the chemical potential of the platelets  $\mu$  and the number density of the spheres  $\rho_s$  [153]. The straight dashed lines are tie-lines illustrating liquid-liquid phase coexistence. The solid and open circles denote the bulk critical point and the wetting transition point, respectively. Between the wetting transition point and the critical point the sphere-rich liquid phase completely wets the interface between a hard substrate and the sphere-poor liquid phase.

as well as due to depletion interactions.

It has been shown that spheres and platelets can be separated by adding a third species to the suspension [155]. The aggregation of platelets ( $R = 0.5 \mu\text{m}$  and  $L = 0.2 \mu\text{m}$ ) and spheres ( $R_s = 0.5 \mu\text{m}$ ) of 1-eicosene wax in a dilute aqueous suspension has been induced by nanometer-sized spherical micelles of sodium dodecyl sulfate. Below the critical micelle concentration neither the platelets nor the spheres aggregate. Upon increasing the micelle concentration the platelets aggregate into columns due to effective entropic attraction while the spheres remain unaggregated. The columnar aggregates of platelets resemble the stacked-coin structures of red blood cells, known as rouleaux, which form when polymers are added to blood. Analogous to fractionated crystallization, the aggregated platelets can be repeatedly separated from the unaggregated spheres by gravitational creaming, yielding a shape-specific colloidal purification method. For high micelle concentrations not only the platelets aggregate but also the spheres aggregate with other spheres. It has been argued that the observed shape-selective colloidal separation might be applicable to a broad class of mixtures of spherical and nonspherical colloids such as viruses, organelles, proteins, and cells [155].

Very recently it has been investigated how the surface roughness of colloidal platelets can affect the depletion attraction between them [156]. The depletion attraction between polymeric pentagonal platelets (pseudo-radius

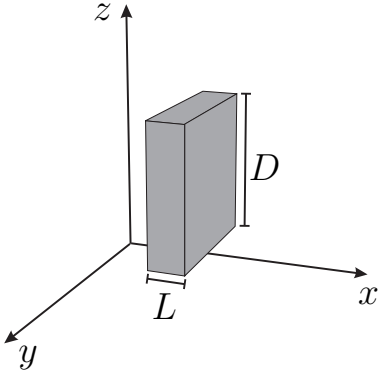


FIG. 14: Within the Zwanzig model, platelets are represented by square parallelepipeds of thickness  $L$  and width  $D$ , which can take only three orientations, along the  $x$ ,  $y$  or  $z$  directions. The number density of the center of mass of the platelet in the figure is denoted by  $\rho_x(\mathbf{r})$ .

$R \approx 1.5 \mu\text{m}$  and thickness  $L = 1 \mu\text{m}$ ) can be suppressed when the nanoscale surface asperity heights on the face of the platelets become larger than the size of nanometer-sized spherical micelles of sodium dodecyl sulfate acting as depletion agent. In the opposite limit, the attraction reappears and columnar stacks of platelets are formed. Exploiting this, the site-specific roughness on only one side of the platelets has been increased in order to form aligned platelet dimers. The two smoother surfaces of two Janus platelets aggregate face-to-face, exposing the rougher surfaces that cannot aggregate. The general problem of how surface roughness affects the strength and range of the depletion attraction is interesting and needs to be elucidated in future.

### E. Density functional theory for the Zwanzig model

Taking into account the simultaneous presence of orientational ordering and polydispersity in density functional calculations for freely rotating nonspherical particles is computationally demanding because the integrals to be evaluated in Eq. (27) are high-dimensional, already within a third-order virial approximation. In order to reduce this computational effort one may use the Zwanzig model for hard square parallelepipeds [157]. Within the Zwanzig model particles of species  $i = 1, \dots, N$  are represented by rectangular blocks of size  $L_i \times D_i \times D_i$ . The positions of the centers of mass vary continuously, while the orientations of the normal of each particle are restricted to discrete directions  $\beta = x, y, z$  (see Fig. 14). Using the notation  $\alpha_x^{(i)}(x, z) = \alpha_i(x, z, \theta = \pi/2, \phi = 0)$ ,  $\alpha_y^{(i)}(x, z) = \alpha_i(x, z, \theta = \pi/2, \phi = \pi/2)$ , and  $\alpha_z^{(i)}(x, z) = \alpha_i(x, z, \theta = 0, \phi = 0)$  for  $\alpha = \rho, U$ , the grand potential functional [Eq. (25)] can be written as

$$\Omega[\{\rho_\beta^{(i)}(\mathbf{r})\}] = F_{id}[\{\rho_\beta^{(i)}(\mathbf{r})\}] + F_{ex}[\{\rho_\beta^{(i)}(\mathbf{r})\}]$$

$$+ \sum_{i=1}^N \sum_{\beta=x,y,z} \int d^3r \rho_\beta^{(i)}(\mathbf{r}) (U_\beta^{(i)}(\mathbf{r}) - \mu_i) \quad (52)$$

with the ideal gas contribution [Eq. (26)]

$$F_{id}[\{\rho_\beta^{(i)}(\mathbf{r})\}] = k_B T \sum_{i=1}^N \sum_{\beta} \int d^3r \rho_\beta^{(i)}(\mathbf{r}) (\ln[\Lambda_i^3 \rho_\beta^{(i)}(\mathbf{r})] - 1). \quad (53)$$

The third-order virial approximation of the excess free energy functional [Eq. (27)] reads

$$F_{ex}[\{\rho_\beta^{(i)}(\mathbf{r})\}] = -\frac{k_B T}{2} \sum_{i,j=1}^N \sum_{\beta_1, \beta_2} \int d^3r_1 d^3r_2 \rho_{\beta_1}^{(i)}(\mathbf{r}_1) f_{\beta_1 \beta_2}^{(ij)}(\mathbf{r}_1, \mathbf{r}_2) \rho_{\beta_2}^{(j)}(\mathbf{r}_2) \times (1 + \frac{1}{3} \sum_{k=1}^2 \sum_{\beta_3} \int d^3r_3 f_{\beta_2 \beta_3}^{(jk)}(\mathbf{r}_2, \mathbf{r}_3) \times \rho_{\beta_3}^{(k)}(\mathbf{r}_3) f_{\beta_3 \beta_1}^{(ki)}(\mathbf{r}_3, \mathbf{r}_1)), \quad (54)$$

where  $f_{\beta_1 \beta_2}^{(ij)}(\mathbf{r}_1, \mathbf{r}_2)$  is the Mayer function which for hard bodies as considered here equals  $-1$  if two particles of species  $i$  and  $j$  with orientations  $\beta_1$  and  $\beta_2$  overlap and is zero otherwise. With the definition

$$S_{\alpha\beta}^{(i)} = D_i + (L_i - D_i) \delta_{\alpha\beta}, \quad (55)$$

which represents the spatial extent in direction  $\alpha = x, y, z$  of a particle of species  $i$  with orientation  $\beta$  of the normal, the Mayer function can be written explicitly as

$$f_{\beta_1 \beta_2}^{(ij)}(\mathbf{r}_1, \mathbf{r}_2) = -\prod_{\alpha} \Theta \left( \frac{1}{2} (S_{\alpha\beta_1}^{(i)} + S_{\alpha\beta_2}^{(j)}) - |r_{\alpha 1} - r_{\alpha 2}| \right), \quad (56)$$

where  $r_{\alpha 1}$  is the projection of the position vector  $\mathbf{r}_1$  in  $\alpha$  direction. The density functional theory is completely specified by the excess free energy functional and the Mayer functions. Minimization of  $\Omega$  with respect to  $\rho_\beta^{(i)}(\mathbf{r})$  leads to integral equations for the equilibrium density profiles.

Zwanzig's model may be considered as a coarse-grained version of the Onsager model, which allows for continuously varying orientations [121, 122]. The model offers the advantage that the determination of phase diagrams and density profiles becomes numerically straightforward, allowing one to study various aspects of platelet fluids in detail and to scan wide parameter ranges. Moreover, Rosenfeld's very successful fundamental measure theory for hard sphere systems has been extended to the Zwanzig model, which is an important alternative in view of the uncertain convergence behavior of the virial series of the equation of state of platelets of finite thickness [158]. Within the fundamental measure theory, one

postulates the following form of the excess free energy functional [159, 160, 161]:

$$F_{ex}[\{\rho_\beta^{(i)}(\mathbf{r})\}] = k_B T \int d^3 r \Phi(\{\rho_\beta^{(i)}(\mathbf{r})\}), \quad (57)$$

with the reduced excess free energy density

$$\Phi = -n_0 \ln(1 - n_3) + \frac{\mathbf{n}_1 \cdot \mathbf{n}_2}{1 - n_3} + \frac{n_{2x} n_{2y} n_{2z}}{(1 - n_3)^2}, \quad (58)$$

and the weighted densities

$$n_l(\mathbf{r}) = \sum_{i=1}^N \sum_{\beta} \int d^3 r_1 \omega_{l\beta}^{(i)}(\mathbf{r} - \mathbf{r}_1) \rho_\beta^{(i)}(\mathbf{r}_1) \quad (59)$$

for  $l \in \{0, 1x, 1y, 1z, 2x, 2y, 2z, 3\}$ . The weight functions  $\omega_{l\beta}^{(i)}(\mathbf{r})$  are obtained by expressing the Fourier transform of the Mayer function [Eq. (56)] as a sum of products of single particle functions. The explicit expressions of the weight functions read:

$$\omega_{0\beta}^{(i)}(\mathbf{r}) = \frac{1}{8} \prod_{\alpha=x,y,z} \delta\left(S_{\alpha\beta}^{(i)}/2 - |r_\alpha|\right), \quad (60)$$

$$\omega_{3\beta}^{(i)}(\mathbf{r}) = \prod_{\alpha=x,y,z} \Theta\left(S_{\alpha\beta}^{(i)}/2 - |r_\alpha|\right), \quad (61)$$

$$\omega_{1\alpha\beta}^{(i)}(\mathbf{r}) = \frac{2\Theta\left(S_{\alpha\beta}^{(i)}/2 - |r_\alpha|\right)}{\delta\left(S_{\alpha\beta}^{(i)}/2 - |r_\alpha|\right)} \omega_{0\beta}^{(i)}(\mathbf{r}), \quad (62)$$

$$\omega_{2\alpha\beta}^{(i)}(\mathbf{r}) = \frac{\delta\left(S_{\alpha\beta}^{(i)}/2 - |r_\alpha|\right)}{2\Theta\left(S_{\alpha\beta}^{(i)}/2 - |r_\alpha|\right)} \omega_{3\beta}^{(i)}(\mathbf{r}). \quad (63)$$

In the limit of monodisperse thin platelets ( $L \ll D$ , see Fig. 14) the excess free energy functional [Eqs. (57) - (63)] reduces to a third-order virial approximation. It is worthwhile to emphasize that the fundamental measure theory for the Zwanzig model yields the exact second and third virial coefficients irrespective of the shape and size polydispersity of the particles. For monodisperse platelets the second virial coefficient is given by Eq. (22) with  $V_p = LD^2$ ,  $A_p = 2D(D+L)$ , and  $\tilde{R}_p = (L+2D)/3$ , while the third virial coefficient reads

$$B_3^{(ZWA)} = V_p^2 + 2\tilde{R}_p A_p V_p + 2A_p^3. \quad (64)$$

As a direct application of the fundamental measure theory one may consider the possibility of an isotropic to nematic phase transition in a monodisperse fluid of platelets, as a function of the aspect ratio  $L/D$ . The broken symmetry in the nematic phase may be characterized by the nematic order parameter [Eq. (45)]:

$$S = \frac{1}{2\rho V} \int d^3 r (2\rho_z(\mathbf{r}) - \rho_x(\mathbf{r}) - \rho_y(\mathbf{r})), \quad (65)$$

where  $\rho = V^{-1} \int d^3 r (\rho_x(\mathbf{r}) + \rho_y(\mathbf{r}) + \rho_z(\mathbf{r}))$ . In the nematic phase  $S = 1$  and  $\rho_x = \rho_y$ . The one-component

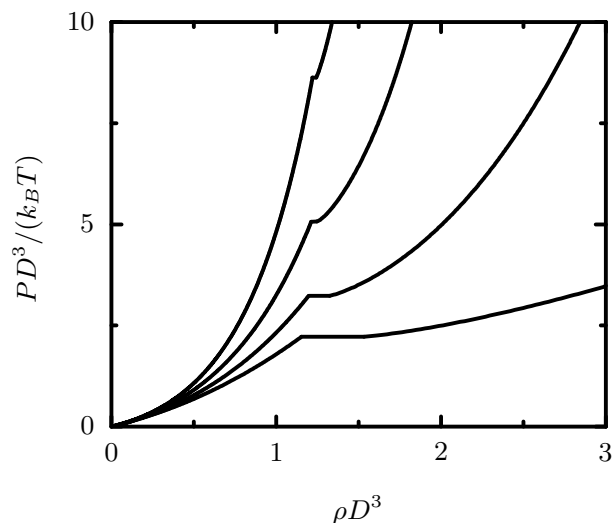


FIG. 15: Equation of state of a monodisperse fluid consisting of rectangular Zwanzig platelets of surface size  $D \times D$  and thickness  $L$  (see Fig. 14 and Eqs. (52) - (63)) for various aspect ratios [158]:  $L/D = 0.01, 0.1, 0.2, 0.3$  (from bottom to top). The horizontal lines are tie-lines illustrating isotropic-nematic two-phase coexistence.

version of the grand potential [Eq. (52)] has been minimized with respect to the order parameter  $S$  for each density  $\rho$  [158]. The resulting equations of state in the isotropic ( $S = 0$ ) and nematic ( $S \neq 0$ ) phases are plotted versus  $\rho$  in Fig. 15, together with the horizontal tie-lines connecting the two phases, for several aspect ratios  $L/D$ . The value of the effective packing fractions  $\phi_I = \rho_I D^3$  and  $\phi_N = \rho_N D^3$  of the coexisting phases are seen to be rather insensitive to the aspect ratio  $L/D$ , while the first-order phase transition narrows as  $L/D$  increases, i.e.,  $\Delta\phi = \phi_N - \phi_I$  decreases with increasing  $L/D$ . The reduced pressure  $PD^3/(k_B T)$ , however, increases rapidly with  $L/D$ , as one might expect.

One may next consider the richer case of highly asymmetric binary mixtures of large and small platelets. Polydispersity, both in diameters and in thickness, is intrinsic to the aforementioned experimental gibbsite samples. In the case of mixtures of spherical colloidal particles large size asymmetry may lead to depletion-induced phase separation. In the case of platelets depletion-induced segregation competes with nematic ordering [162], as is also the case for mixtures of long and short rods, or of thin and thick rods. Figure 16 displays a phase diagram of binary mixtures of square platelets constructed as function of the chemical potential  $\mu_2$  of the small platelets and the number density  $\rho_1$  of the large platelets ( $D_1 > D_2$ ). The tie-lines are horizontal because of equality of  $\mu_2$  of the coexisting phases. For large negative chemical potential  $\mu_2$ , the systems exhibit a first-order isotropic (I) to nematic (N) phase transition and the density gap at the isotropic to nematic phase transition broadens with increasing  $\mu_2$  in agreement with calculations for binary mixtures of in-



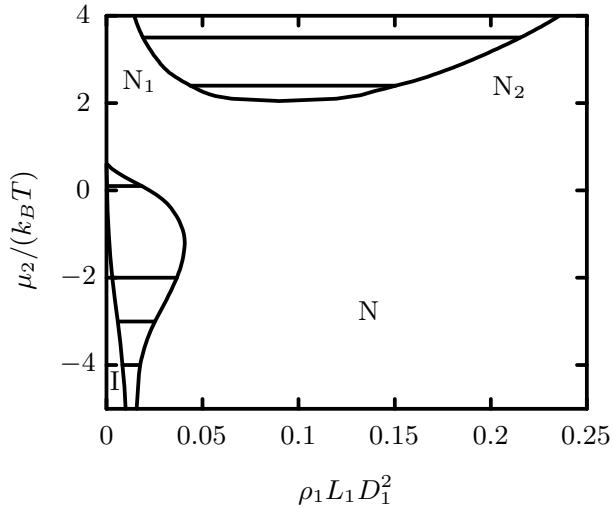


FIG. 16: Phase diagram of a fluid consisting of a binary mixture of large thin Zwanzig platelets [ $L_1/D_1 = 0.01$ ] and small Zwanzig platelets [ $D_1/D_2 = 2$ ,  $L_2/D_2 = 0.16$ ] according to Eqs. (52) - (63) as a function of the chemical potential of the small platelets  $\mu_2$  and the density of the large platelets  $\rho_1$  [158]. The straight solid lines are tie-lines illustrating isotropic-nematic (I-N) and nematic-nematic ( $N_1$ - $N_2$ ) two-phase coexistence, respectively. The chemical potential at I-N coexistence of a monodisperse fluid consisting of the small platelets is  $\mu_2/(k_B T) = 0.68$ .

finitely thin platelets [163]. At high densities in the nematic phase, the small platelets are nearly excluded and hence the large platelets are in equilibrium with a reservoir of small platelets. This implies that the pressure of the nematic phase is equal to that of a reservoir of small platelets at a chemical potential  $\mu_2$ . The isotropic-nematic two-phase coexistence regime is bounded by an upper critical point above which a single stable nematic phase is found. The nematic phase demixes into two nematic phases ( $N_1$ ,  $N_2$ ) at sufficiently large values of  $\mu_2$ .

Upon increasing the aspect ratio  $L_2/D_2$  of the small platelets at fixed  $L_1$  and  $D_1$ , the lower critical point of the nematic-nematic two-phase coexistence region shifts to smaller values of  $\mu_2$ , until the nematic-nematic and isotropic-nematic two-phase coexistence regions start to overlap, giving rise to a triple point at which two nematic phases ( $N_1$ ,  $N_2$ ) coexist with an isotropic phase [158].

Figure 17 displays an alternative representation of the phase diagram shown in Fig. 16 in terms of the number densities of the large and the small platelets  $\rho_1$  and  $\rho_2$ , respectively. The figure illustrates how the composition of the mixture varies upon increasing the chemical potential (and hence the reservoir density) of the small platelets. Whereas the density of the thin platelets  $\rho_1$  is always smaller in the isotropic phase than in the nematic phase along the coexistence curve, a density inversion for the thick platelets has been found. The density of the thick platelets  $\rho_2$  is larger in the isotropic phase than in the coexisting nematic phase for small chemi-

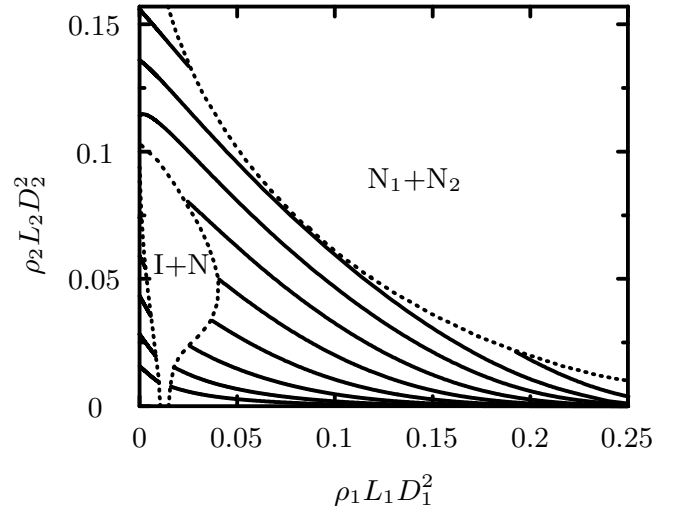


FIG. 17: Phase diagram of a binary platelet fluid, corresponding to Fig. 16, in the density-density, i.e.,  $\rho_1$ - $\rho_2$  plane [158]. The dotted lines indicate phase boundaries. The chemical potential of the small thick platelets is kept fixed for each solid line and increases from bottom to top:  $\mu_2/(k_B T) = -5, -4, -3, -2, -1, 0, 1, 1.9, 3$ .

cal potentials  $\mu_2$ , while  $\rho_2$  is smaller in the isotropic phase than in the coexisting nematic phase for large chemical potentials  $\mu_2$ . This remarkable phenomenon of isotropic-nematic density inversion has been observed experimentally for a dispersion of sterically stabilized gibbsite platelets [11]. The calculated density profile  $\rho_2(z)$  of thick platelets at the isotropic-nematic interface exhibits oscillations [164]. The interfacial tension for platelets with their mean bulk orientation parallel to the interface is smaller than for the corresponding perpendicular configuration. The calculated interfacial tension  $\gamma \approx 10$  nN/m for gibbsite platelets agrees with the measured value [10, 165]. Both the large platelet and small platelet density profiles exhibit pronounced oscillations on one side of the nematic-nematic interface, provided the chemical potentials are sufficiently high. Upon approaching the lower critical point of the nematic-nematic demixing region (see Fig. 16) the oscillations vanish at a Fisher-Widom line and the interface broadens [164].

A second-order virial approximation [Eq. (54), without the last term] has been used to investigate the phase diagram of binary mixtures of rods and platelets [166, 167]. It has been found that mixing rods and platelets can stabilize a biaxial nematic phase in which the symmetry axes of particles of different species point along mutually perpendicular directions. This phase behavior was later confirmed in calculations for a polydisperse mixture of rods and platelets using fundamental measure theory [168]. A virial approximation has also been used to study wetting and capillary nematization of platelet and rod fluids in contact with planar and geometrically structured substrates [163, 169]. The predicted complete wetting of the

substrate-isotropic liquid interface by a uniaxial nematic platelet film has been found later in a colloidal dispersion of sterically stabilized gibbsite platelets [165]. The wetting behavior of the nematic gibbsite phase has been revealed by polarized light microscopy.

The relaxation dynamics of Zwanzig platelets has been investigated by means of dynamic density functional theory [170]. The driving force for time dependence has been expressed in terms of gradients of the local chemical potential. The formalism has been applied to model an initially homogeneous stable or metastable isotropic fluid which is perturbed by switching a two-dimensional array of Gaussian laser beams. Switching on the laser beams leads to an accumulation of platelets in the beam centers. If the initial chemical potential and the laser power are large enough, a preferred orientation of the particles occurs, breaking the symmetry of the laser potential. After switching off the laser beams again, the system can follow different relaxation paths. It either relaxes back to the homogeneous isotropic state or it forms an approximately elliptical high-density core which is elongated perpendicular to the dominating orientation in order to minimize the surface free energy. For large supersaturations of the initial isotropic fluid, the high-density cores of neighboring laser beams of the two-dimensional array merge into complex superstructures.

Recently, nonequilibrium steady states in an open system connecting two reservoirs of platelike colloidal particles have been investigated using a dynamic density functional theory for the Zwanzig model [171]. Inhomogeneities of the local chemical potential generate a diffusion current which relaxes to a nonvanishing value if the two reservoirs coupled to the system sustain different chemical potentials. The relaxation process of initial states towards the steady state turned out to comprise two regimes: a smoothening of initial steplike structures followed by an ultimate relaxation of the slowest diffusive mode. The position of a nonequilibrium interface and the particle current of steady states depends nontrivially on the structure of the reservoirs due to the coupling between translational and orientational degrees of freedom of the fluid.

#### F. Equilibrium properties of charged Zwanzig platelets

Bulk properties and free interfaces of mixtures of charged platelets and salt have been studied within the density functional theory for the Zwanzig model [172]. The excess free energy functional has been decomposed into the fundamental measure contribution [Eq. (57)] and an electrostatic part which has been derived by functional integration of an extension of the Debye-Hückel pair distribution function with respect to the interaction potential. The calculations have shown that the isotropic and nematic binodals are shifted to higher platelet densities upon increasing the platelet charge. The Donnan poten-

tial between the coexisting isotropic and nematic phases has been inferred from bulk structure calculations. Non-monotonic density and nematic order parameter profiles have been found at a free interface interpolating between the coexisting isotropic and nematic phases. Moreover, electrically charged layers form at the free interface leading to monotonically varying electrostatic potential profiles. For fixed salt density, the interfacial tension decreases upon increasing the macroion charge.

Analytically and numerically calculated surface phase diagrams of charged Zwanzig platelets and salt in contact with a charged planar substrate exhibit first-order wetting for sufficiently small platelet charges and isotropic bulk order as well as first-order drying for sufficiently large platelet charges and nematic bulk order [173]. A crossover from monotonic to nonmonotonic electrostatic potential profiles upon varying the surface charge density has been observed. Nonmonotonic electrostatic potential profiles are equivalent to the occurrence of charge inversion. Due to the presence of both the Coulomb interactions and the hard-core repulsions, the surface potential and the surface charge do not vanish simultaneously, i.e., the point of zero charge and the isoelectric point of the surface do not coincide.

## VI. SPATIALLY INHOMOGENEOUS BULK PHASES

The Zwanzig model offers the advantage that the difficult determination of spatially inhomogeneous bulk phases becomes numerically feasible [164, 174, 175, 176]. The predicted phase behavior is in qualitative agreement with the results obtained for freely rotating parallelepipeds using computer simulations [177]. In order to find spatially inhomogeneous bulk phases such as columnar and smectic phases, the spatially homogeneous solutions of the Euler-Lagrange equations for the fundamental measure theory of the Zwanzig model [Eqs. (52) - (63)] are perturbed by adding a narrow Lorentz peak and iterated using a Picard scheme. If the latter converges towards the spatially homogeneous solution (isotropic or nematic phase), one concludes that this is indeed the equilibrium state because it is stable under density variations. This method is the numerical analog of a bifurcation analysis since a narrow Lorentz peak has a broad Fourier spectrum. In the case of the phase diagram for the binary mixtures of large thin and small thick platelets shown in Figs. 16 and 17 it has been found that the nematic phase  $N_1$  undergoes a phase transition into a columnar phase, where parallel columns of small platelets are surrounded by single platelets with orientations perpendicular to the column axis [164]. For small values of  $\rho_1$ , the nematic to columnar phase transition is weakly first-order. The nematic-columnar boundary line changes to strongly first-order at the tricritical point where the nematic-nematic boundary line ends.

Over the past few years, spatially homogeneous and

inhomogeneous bulk phases of the aforementioned suspensions of colloidal gibbsite platelets have been investigated. For example, van der Kooij et al. [9] have studied two systems which differ by the degree of polydispersity of the radius of the platelets (17 % and 25 %, respectively). The phase behavior of the platelet suspensions as function of the volume fraction  $\phi$  of the platelets is shown in Fig. 18. Isotropic-nematic two-phase coexistence has been observed just below  $\phi = 0.2$ , yielding an isotropic upper phase and a birefringent nematic bottom phase in the tubes containing the suspensions. Macroscopic phase separation has been found to be complete within 12 hours. The width of the biphasic gap  $\Delta\phi = \phi_N - \phi_I$  increases with increasing the degree of polydispersity of the platelet radius. Upon increasing the volume fraction of the platelets to  $\phi \approx 0.4$ , both suspensions enter a biphasic region where a nematic phase coexists with a more concentrated birefringent columnar phase. A comparison of the experimentally observed volume fractions at the isotropic to nematic and nematic to columnar phase transitions with computer simulation data for monodisperse platelets [117] has shown that the transitions in the experiment are shifted to lower volume fractions which might be due the polydispersity in size and shape of the gibbsite platelets [9]. The stability of the observed columnar phase is remarkable in view of predictions for the terminal size polydispersity of about 10 % for the crystal phase of hard spheres and the terminal length polydispersity of about 18 % for the smectic phase of hard rods. Small-angle x-ray scattering has revealed a hexagonal intercolumnar ordering in the columnar phase [178]. The system forms a powder consisting of true long-range-ordered columnar crystallites, where the relatively large free space between the columns allows for the accommodation of rather highly polydisperse platelets. However, under the influence of gravitational compression very little space is available. The geometrical frustration induced by the platelet polydispersity can suppress the ordering upon increasing density and favor hexaticlike structuring. The resulting novel columnar phase has been found at the bottom of a tube containing a gibbsite suspension [178]. The hexatic phase is characterized by short-range translational order while its bond-orientational order is long ranged.

Moreover, polydisperse colloidal gibbsite platelets have been reported to form an opal-like columnar crystal with iridescent Bragg reflections [20]. It has been shown that the formation process of the iridescent phase under slow sedimentation can be accelerated by orders of magnitude using a centrifugation without arresting the system in a disordered glassy state. It has been argued that the formation of the hexatic phase with a finite position correlation length may play a role in the self-organization of the platelets [20].

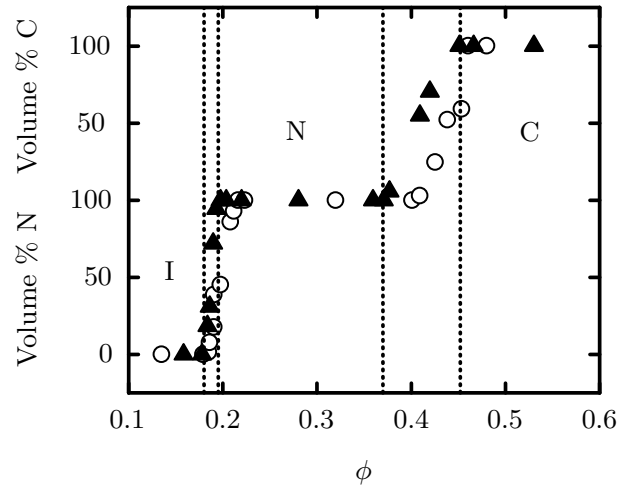


FIG. 18: Phase diagram of two gibbsite suspensions which differ by the degree of polydispersity of the platelet radius (triangles, 17 % and circles, 25 %) [9]. The relative volume fraction of the nematic (N) and columnar (C) phase are plotted as function of the platelet volume fraction  $\phi$ . For low volume fraction the isotropic phase (I) is stable. The dotted lines mark the boundaries of the two-phase coexistence regions of the system with 17 % polydispersity of the platelet radius.

## VII. SUMMARY AND OUTLOOK

This work has been devoted to the investigation of the structure and thermodynamics of platelet dispersions. The shape of the particles and the polydispersity in size can be revealed by cryogenic transmission electron microscopy [Fig. 1] and the form factor [Eqs. (1) - (4)] measured by light scattering, small-angle neutron scattering, or small-angle x-ray scattering [Figs. 3 and 4]. The combination of these methods has demonstrated that well-defined and perfectly dispersed single lamellar nanoplatelets of the cheapest polyolefin, namely polyethylene, can be made in water [1]. Due to their unusual size, structure, and thermal history, these platelets will contribute to fundamental and long-standing issues of polymer crystallization [2].

The interaction site integral equation theory [Eqs. (5) - (13)] is quite successful in describing experimental structure factors of fluids containing uncharged platelets [Fig. 5] or uniformly charged platelets [Fig. 6]. Rigid dendrimers [Fig. 2] may serve as model systems for interacting monodisperse particles in statistical physics [36], while the colloidal platelets synthesized so far are highly polydisperse in size.

The inverse structure factor extrapolated to vanishing scattering vectors as predicted by both scaled particle theory and fundamental measure theory is systematically smaller than the experimental data for platelike stilbenoid dendrimers of the third generation and the prediction of the interaction site integral equation theory

[Fig. 9 and Eqs. (18) - (24)]. The substantial differences observed between the experimental data and the results of scaled particle theory and fundamental measure theory confirm earlier caveats concerning the applicability of these theories to freely rotating nonspherical particles [112] and are due to the fact that both theories do not yield the correct third virial coefficient. Hence there is a clear need to improve both scaled particle theory and fundamental measure theory for platelets.

The different charge densities on the rim and the face of laponite platelets may lead the significant difference between the effective pair potentials and structure factors of laponite and polyelectrolytes [Figs. 7 and 8]. However, at the present stage there is no definite answer to this issue because no theoretical calculations are available yet. An integral equation approach based on the reference interaction site model with different charges on the face and the rim of the platelets is expected to be helpful for the understanding of the microscopic structure of laponite suspensions. An important point that is common to many experimental studies of laponite suspensions is the analysis of obvious nonequilibrium states reached after passing the gel line. As a matter of fact, considerable efforts have been devoted to the investigation of the exact position of the gel line. The experimental difficulties of the investigation of such time-dependent states are at hand. Moreover, no clear information on the nature of the interparticle interaction potential can be derived from essentially nonequilibrium states.

Density functional theory [Eqs. (25) - (34)] has been used to study the phase behavior of thin hard platelets [Fig. 10] in three dimensions. The system exhibits a first-order isotropic to nematic phase transition with a small density jump at two-phase coexistence and a rather low nematic order parameter in the nematic phase. Within a geometry-based density functional theory the excess free energy is expressed in terms of weighted densities [Eqs. (35) - (43)]. However, this fundamental measure theory does not yield the correct third virial coefficient due to the occurrence of lost cases. These lost cases can be compensated by overcounting the cases with triple intersection such that the resulting equation of state in both the isotropic and the nematic phase as well as the location of the isotropic to nematic phase transition agree with computer simulation data [Fig. 11].

Density functional theory has also been used to study binary colloidal fluids consisting of hard spheres and thin platelets in their bulk and near a planar hard substrate. This system exhibits liquid-liquid coexisting of a phase that is rich in spheres (poor in platelets) and a phase that is poor in spheres (rich in spheres) [Fig 13]. An interesting issue that has not been addressed theoretically is how the roughness of platelets modifies depletion interactions [156].

Although the particle shape is equivalent, overlapping pair configurations are different for freely rotating platelets in three dimension as compared to the strictly two-dimensional case. Fundamental measure

theory yields only an approximate expression for the Mayer function of strictly two-dimensional hard platelets [Fig. 12]. The understanding of the deconvolution of the Mayer function for platelets in two dimensions needs to be improved [179].

Zwanzig's model of parallelepipeds with only three allowed orientations [Fig. 14] has been generalized to the case of monodisperse, bidisperse, and polydisperse systems of platelets. In view of the uncertainties concerning the convergence of the virial series [Eqs. (52) - (56)], a fundamental measure theory has been used to derive a free energy functional [Eqs. (57) - (63)]. This fundamental measure theory for the Zwanzig model yields the exact second and third virial coefficients irrespective of the shape and size polydispersity of the particles. In the monodisperse case, the isotropic to nematic phase transition narrows with increasing aspect ratio of the platelets [Fig. 15]. The bulk phase diagram for a representative example of binary hard platelet fluids [Figs. 16 and 17] involve an isotropic and one or two nematic phases of different concentrations as well as a columnar phase.

The Zwanzig model offers the advantage that the difficult determination of spatially inhomogeneous bulk phases and density profiles becomes numerically feasible. The calculated low interfacial tensions are in agreement with experimental data for gibbsite platelets. Moreover, the predicted wetting behavior of platelet fluids in contact with substrates has been confirmed experimentally [165]. It is appealing to base the construction of theories for the dynamics of platelets on the equilibrium fundamental measure functional for the Zwanzig model [170]. In addition to the technological relevance of this issue (e.g., sediment transport processes in hydraulic engineering), the investigation of dynamic properties of platelet fluids provides the opportunity to study the coupling of translational and rotational motion as well as the time dependence of the orientation of particles induced by external fields.

The liquid-crystalline phase behavior of colloidal gibbsite platelets has been studied over the past few years. It has been observed that suspensions of both sterically and charge-stabilized gibbsite platelets at sufficiently high concentrations display iridescence. From small-angle x-ray scattering experiments it follows that these iridescent phases have a columnar structure [Fig. 18] with hexagonal intercolumnar ordering. This is quite remarkable because the gibbsite platelets have a polydispersity of 19 % in diameter and 27 % in thickness. In general, size polydispersity of colloidal particles is expected to suppress the formation of ordered phases.

For the case of monodisperse hard platelets an accurate description of a columnar liquid crystal phase at high packing fractions has been presented using an improved free volume theory [180, 181]. It has been shown that orientational entropy of the platelets in the one-dimensional columns leads to a different high-density pressure compared to the prediction from traditional cell theory. Quantitative agreement has been found with

Monte Carlo simulation results for various thermodynamic properties. In view of this progress made in developing an accurate descriptions of a columnar liquid crystal consisting of monodisperse hard platelets, future work may focus on the understanding of the influence of platelet size polydispersity, gravity, and external fields on the phase behavior. Discotic liquid crystal science is still a rather young research field compared with the more developed field of liquid crystals consisting of rod-

like molecules. Nevertheless, many applications for discotic liquid systems in areas such as photovoltaic and optical compensation films for displays have been investigated over the last years. However, the microscopic understanding of the properties of columnar phases and the alignment at surfaces needs to be improved in particular in view of the emerging research area of smart low-dimensional building blocks consisting of discotic liquid crystals.

- 
- [1] C. H. M. Weber, A. Chiche, G. Krausch, S. Rosenfeldt, M. Ballauff, L. Harnau, I. Göttker-Schnetmann, Q. Tong, and S. Mecking, *Nano Letters* **7**, 2024 (2007).
- [2] S. Z. D. Cheng, *Nature* **448**, 1006 (2007).
- [3] A. B. D. Brown, S. M. Clarke, and A. R. Rennie, *Langmuir* **14**, 3129 (1998).
- [4] A. B. D. Brown, C. Ferrero, T. Narayanan, and A. R. Rennie, *Eur. Phys. J. B* **11**, 481 (1999).
- [5] F. M. van der Kooij and H. N. W. Lekkerkerker, *J. Phys. Chem. B* **102**, 7829 (1998).
- [6] F. M. van der Kooij and H. N. W. Lekkerkerker, *Phys. Rev. Lett.* **84**, 781 (2000).
- [7] F. M. van der Kooij and H. N. W. Lekkerkerker, *Langmuir* **16**, 10144 (2000).
- [8] F. M. van der Kooij, M. Vogel, and H. N. W. Lekkerkerker, *Phys. Rev. E* **62**, 5397 (2000).
- [9] F. M. van der Kooij, K. Kassapidou, and H. N. W. Lekkerkerker, *Nature* **406**, 868 (2000).
- [10] F. M. van der Kooij and H. N. W. Lekkerkerker, *Phil. Trans. R. Soc. Lond. A* **359**, 985 (2001).
- [11] F. M. van der Kooij, D. van der Beek, and H. N. W. Lekkerkerker, *J. Phys. Chem. B* **105**, 1696 (2001).
- [12] D. van der Beek and H. N. W. Lekkerkerker, *Europhys. Lett.* **61**, 702 (2003).
- [13] D. van der Beek and H. N. W. Lekkerkerker, *Langmuir* **20**, 8582 (2004).
- [14] D. van der Beek, T. Schilling, and H. N. W. Lekkerkerker, *J. Chem. Phys.* **121**, 5423 (2004).
- [15] D. van der Beek, A. V. Petukhov, S. M. Oversteegen, G. J. Vroege, and H. N. W. Lekkerkerker, *Eur. Phys. J. E* **16**, 253 (2005).
- [16] J. E. G. J. Wijnhoven, *J. Colloid Interface Sci.* **292**, 403 (2005).
- [17] J. E. G. J. Wijnhoven, D. D. van't Zand, D. van der Beek, and H. N. W. Lekkerkerker, *Langmuir* **21**, 10422 (2005).
- [18] D. van der Beek, A. V. Petukhov, P. Davidson, J. Ferre, J. P. Jamet, H. H. Wensink, G. J. Vroege, W. Bras, and H. N. W. Lekkerkerker, *Phys. Rev. E* **73**, 041402 (2006).
- [19] M. C. D. Mourad, J. E. G. J. Wijnhoven, D. D. van't Zand, D. van der Beek, and H. N. W. Lekkerkerker, *Phil. Trans. R. Soc. Lond. A* **364**, 2807 (2006).
- [20] D. van der Beek, P. B. Radstake, A. V. Petukhov, and H. N. W. Lekkerkerker, *Langmuir* **23**, 11343 (2007).
- [21] S. Chen and D. L. Carroll, *J. Phys. Chem. B* **108**, 5500 (2004).
- [22] J. Li, Y. Qin, X. Kou and J. Huang, *Nanotechnology* **15**, 982 (2004).
- [23] J. Li, Y. Qin, X. Kou, and J. Huang, *J. Nanoscience and Nanotechnology* **5**, 1699 (2005).
- [24] J. Zhang, L. Luan, W. Zhu, S. Liu and D. Sun, *Langmuir* **23**, 5331 (2007).
- [25] M. Ballauff and C. N. Likos, *Angew. Chem. Int. Ed.* **43**, 2998 (2004).
- [26] H. Meier and M. Lehmann, *Angew. Chem.* **110**, 666 (1998); *Angew. Chem. Int. Ed.* **37**, 643 (1998).
- [27] K. Müllen, A. J. Berresheim, and M. Müller, *Chem. Rev.* **99**, 1747 (1999).
- [28] H. Meier, M. Lehmann, and U. Kolb, *Chem. Eur. J.* **6**, 2462 (2000).
- [29] M. Wind, K. Saalwächter, U.-M. Wiesler, K. Müllen, and H. W. Spiess, *Macromolecules* **35**, 10071 (2002).
- [30] H. Meier, E. Karpuk, M. Lehmann, D. Schollmeyer, and V. Enkelmann, *Z. Naturforsch. B* **58**, 775 (2003).
- [31] S. Rosenfeldt, N. Dingenouts, D. Pötschke, M. Ballauff, A. J. Berresheim, K. Müllen, and P. Lindner, *Angew. Chem.* **116**, 111 (2004); *Angew. Chem. Int. Ed.* **43**, 109 (2004).
- [32] S. Rosenfeldt, N. Dingenouts, D. Pötschke, M. Ballauff, A. J. Berresheim, K. Müllen, P. Lindner, and K. Saalwächter, *J. Lumin.* **111**, 225 (2005).
- [33] P. Carbone, A. Calabretta, M. D. Stefano, F. Negri, and K. Müllen, *J. Phys. Chem. A* **110**, 2214 (2006).
- [34] A. Schulz and H. Meier, *Tetrahedron* **63**, 11429 (2007).
- [35] S. Rosenfeldt, E. Karpuk, M. Lehmann, H. Meier, P. Lindner, L. Harnau, and M. Ballauff, *ChemPhysChem* **7**, 2097 (2006).
- [36] L. Harnau, S. Rosenfeldt, and M. Ballauff, *J. Chem. Phys.* **127**, 014901 (2007).
- [37] J. D. F. Ramsay, *J. Colloid Interface Sci.* **109**, 441 (1986).
- [38] J. D. F. Ramsay, S. W. Swanton, and J. Bunce, *J. Chem. Soc. Faraday Trans.* **86**, 3919 (1990).
- [39] J. D. F. Ramsay and P. Lindner, *J. Chem. Soc. Faraday Trans.* **89**, 4207 (1993).
- [40] F. R. C. Chang and G. Sposito, *J. Colloid Interface Sci.* **163**, 19 (1994).
- [41] A. Mourchid, A. Delville, J. Lambard, E. Lecollier, and P. Levitz, *Langmuir* **11**, 1942 (1995).
- [42] M. Kroon, G. Wegdam, and R. Sprik, *Phys. Rev. E* **54**, 6541 (1996).
- [43] E. Trizac and J.-P. Hansen, *Phys. Rev. E* **56**, 3137 (1997).
- [44] J.-P. Hansen and E. Trizac, *Physica A* **235**, 257 (1997).
- [45] J.-P. Hsu and M.-T. Tseng, *Langmuir* **13**, 1810 (1997).
- [46] M. Dijkstra, J.-P. Hansen, and P. A. Madden, *Phys. Rev. E* **55**, 3044 (1997).
- [47] M. Kroon, W. L. Vos, and G. H. Wegdam, *Phys. Rev. E* **57**, 1962 (1998).
- [48] A. Mourchid, E. Lecollier, H. van Damme, and P.

- Levitz, *Langmuir* **14**, 4718 (1998).
- [49] A. Mourchid and P. Levitz, *Phys. Rev. E* **57**, R4887 (1998).
- [50] A. Delville, *J. Phys. Chem. B* **103**, 8296 (1999).
- [51] D. Bonn, H. Tanaka, G. Wegdam, H. Kellay, and J. Meunier, *Europhys. Lett.* **45**, 52 (1999).
- [52] D. Bonn, H. Kellay, H. Tanaka, G. Wegdam, and J. Meunier, *Langmuir* **15**, 7534 (1999).
- [53] D. G. Rowan, J.-P. Hansen, and E. Trizac, *Molec. Phys.* **98**, 1369 (2000).
- [54] S. Kutter, J.-P. Hansen, M. Sprik, and E. Boek, *J. Chem. Phys.* **112**, 311 (2000).
- [55] A. Knaebel, M. Bellour, J. P. Munch, V. Viasnoff, F. Lequeux, and J. M. Harden, *Europhys. Lett.* **52**, 73 (2000).
- [56] B. Abou, D. Bonn, and J. Meunier, *Phys. Rev. E* **64**, 021510 (2001).
- [57] L. Harnau, D. Costa, and J.-P. Hansen, *Europhys. Lett.* **53**, 729 (2001).
- [58] T. Nicolai and S. Cocard, *Eur. Phys. J. E.* **5**, 221 (2001).
- [59] T. Nicolai and S. Cocard, *J. Colloid Interface Sci.* **244**, 51 (2001).
- [60] D. Bonn, S. Tanase, B. Abou, H. Tanaka, and J. Meunier, *Phys. Rev. Lett.* **89**, 015701 (2002).
- [61] E. Trizac, L. Bocquet, R. Agra, J.-J. Weis and M. Aubouy, *J. Phys. Cond. Mat.* **14**, 9339 (2002).
- [62] C. Martin, F. Pignon, J.-M. Piau, A. Magnin, P. Lindner, and B. Cabane, *Phys. Rev. E* **66**, 021401 (2002).
- [63] M. Bellour, A. Knaebel, J. L. Harden, F. Lequeux, and J.-P. Munch, *Phys. Rev. E* **67**, 031405 (2003).
- [64] R. Agra, E. Trizac, and L. Bocquet, *Eur. Phys. J. E.* **15**, 345 (2004).
- [65] H. Tanaka, J. Meunier, and D. Bonn, *Phys. Rev. E* **69**, 031404 (2004).
- [66] P. Mongondry, T. Nicolai, and J.-F. Tassin, *J. Colloid Interface Sci.* **275**, 191 (2004).
- [67] B. Ruzicka, L. Zulian, and G. Ruocco, *J. Phys.: Condens. Matter* **16**, S4993 (2004).
- [68] R. Bandyopadhyay, D. Liang, H. Yardimci, D. A. Sessoms, M. A. Borthwick, S. G. J. Mochrie, J. L. Harden, and R. L. Leheny, *Phys. Rev. Lett.* **93**, 228302 (2004).
- [69] G. Odriozola, M. Romero-Bastida, and F. de J. Guevara-Rodriguez, *Phys. Rev. E* **70**, 021405 (2004).
- [70] H. Tanaka, S. Jabbari-Farouji, J. Meunier, and D. Bonn, *Phys. Rev. E* **71**, 021402 (2005).
- [71] P. Mongondry, J. F. Tassin, and T. Nicolai, *J. Colloid Interface Sci.* **283**, 397 (2005).
- [72] B. Ruzicka, L. Zulian, and G. Ruocco, *Langmuir* **22**, 1106 (2006).
- [73] F. Schosseler, S. Kaloun, M. Skouri, and J. P. Munch, *Phys. Rev. E* **73**, 021401 (2006).
- [74] A. Delville, *J. Phys. Chem. B*, **110**, 11950 (2006).
- [75] C. Martin, F. Pignon, A. Magnin, M. Meireles, V. Lelievre, P. Lindner, and B. Cabane, *Langmuir* **22**, 4065 (2006).
- [76] S. Mossa, C. De Michele, and F. Sciortino, *J. Chem. Phys.* **126**, 014905 (2007).
- [77] H. Z. Cummins, *J. Non-Cryst. Solids* **353**, 3891 (2007).
- [78] F. Ianni, R. Di Leonardo, S. Gentilini, and G. Ruocco, *Phys. Rev. E* **75**, 011408 (2007).
- [79] B. Ruzicka, L. Zulian, and G. Ruocco, *Phil. Mag.* **87**, 449 (2007).
- [80] S. Jabbari-Farouji, G. H. Wegdam, and D. Bonn, *Phys. Rev. Lett.* **99**, 065701 (2007).
- [81] I. Bihannic, L. J. Michot, B. S. Lartiges, D. Vantelon, J. Labille, F. Thomas, J. Susini, M. Salome, and B. Fayard, *Langmuir* **17**, 4144 (2001).
- [82] E. Balnois, S. Durand-Vidal, and P. Levitz, *Langmuir* **19**, 6633 (2003).
- [83] N. N. Herrera, J.-M. Letoffe, J.-L. Putaux, L. David, and E. Bourgeat-Lami, *Langmuir* **20**, 1564 (2004).
- [84] E. S. H. Leach, A. Hopkinson, K. Franklin, and J. S. van Duijneveld, *Langmuir* **21**, 3821 (2005).
- [85] L. Li, L. Harnau, S. Rosenfeldt, and M. Ballauff, *Phys. Rev. E* **72**, 051504 (2005).
- [86] D. Chandler and H. C. Andersen, *J. Chem. Phys.* **57**, 1930 (1972).
- [87] D. Chandler in *Studies in Statistical Mechanics*, edited by J. L. Lebowitz and E. W. Montroll, Vol. 8, p. 275, (North Holland, Amsterdam, 1982).
- [88] J.-P. Hansen and I. R. McDonald, *Theory of Simple Liquids* (Academic Press, London, 1986).
- [89] P. A. Monson and G. P. Morriss, *Adv. Chem. Phys.* **77**, 451 (1990).
- [90] K. S. Schweizer and J. G. Curro, *Phys. Rev. Lett.* **58**, 246 (1987).
- [91] A. Yethiraj and C.-Y. Shew, *Phys. Rev. Lett.* **77**, 3937 (1996).
- [92] A. Yethiraj and C.-Y. Shew, *J. Chem. Phys.* **106**, 5706 (1997).
- [93] C.-Y. Shew and A. Yethiraj, *J. Chem. Phys.* **109**, 5162 (1998).
- [94] L. Harnau and P. Reineker, *J. Chem. Phys.* **112**, 437 (2000).
- [95] K. S. Schweizer and J. G. Curro, *Adv. Chem. Phys.* **98**, 1 (1997).
- [96] L. Harnau, *J. Chem. Phys.* **115**, 1943 (2001).
- [97] L. Harnau and J.-P. Hansen, *J. Chem. Phys.* **116**, 9051 (2002).
- [98] S. Bolisetty, C. Airaud, Y. Xu, A. H. E. Müller, L. Harnau, S. Rosenfeldt, P. Lindner, and M. Ballauff, *Phys. Rev. E* **75**, 040803(R) (2007).
- [99] K. Henzler, S. Rosenfeldt, A. Wittmann, L. Harnau, S. Finet, T. Narayanan, and M. Ballauff, *Phys. Rev. Lett.* **100**, 158301 (2008).
- [100] D. Costa, J.-P. Hansen, and L. Harnau, *Molec. Phys.* **103**, 1917 (2005).
- [101] D. Laria, D. Wu, and D. Chandler, *J. Chem. Phys.* **95**, 4444, (1991).
- [102] B. Ruzicka, L. Zulian, and G. Ruocco, *Phys. Rev. Lett.* **93**, 258301 (2004).
- [103] R. Piazza, *Curr. Opin. Colloid Interface Sci.* **5**, 38 (2000).
- [104] G. Pellicane, D. Costa, and C. Caccamo, *J. Phys.: Condens. Matter* **15**, 375 (2003).
- [105] F. Sciortino, S. Mossa, E. Zaccarelli, and P. Tartaglia, *Phys. Rev. Lett.* **93**, 055701 (2004).
- [106] D. Ruelle, *Statistical Mechanics: Rigorous Results*, (Imperial, London, 1969).
- [107] K. Kassapidou, W. Jesse, M. E. Kuil, A. Lapp, S. Egelhaaf, and J. R. C. van der Maarel, *Macromolecules* **30**, 2671 (1997).
- [108] D. P. Norwood, M. Benmouna, and W. F. Reed, *Macromolecules* **29**, 4293 (1996).
- [109] E. E. Maier, S. F. Schulz, and R. Weber, *Macromolecules* **21**, 1544 (1988).
- [110] M. A. Cotter in *Molecular Physics of Liquid Crystals*, edited G. R. Luckhurst and G. W. Gray, p. 169, (Aca-

- demic Press, London, 1979).
- [111] B. M. Mulder and D. Frenkel, *Molec. Phys.* **55**, 119 (1985).
  - [112] S. M. Oversteegen and R. Roth, *J. Chem. Phys.* **122**, 214502 (2005).
  - [113] K. L. Savithramma and N. V. Madhusudana, *Molec. Cryst. Liq. Cryst.*, **74**, 243 (1981).
  - [114] T. Boublik, *J. Chem. Phys.* **63**, 4084 (1975).
  - [115] D. Frenkel and R. Eppenga, *Phys. Rev. E* **49**, 1089 (1982).
  - [116] R. Eppenga and D. Frenkel, *Molec. Phys.* **52**, 1303 (1984).
  - [117] J. A. C. Veerman and D. Frenkel, *Phys. Rev. A* **45**, 5632 (1992).
  - [118] M. A. Bates and D. Frenkel, *J. Chem. Phys.* **110**, 6553 (1999).
  - [119] S.-D. Zhang, P. A. Reynolds, and J. S. van Duijneveldt, *Molec. Phys.* **100**, 3041 (2002).
  - [120] S.-D. Zhang, P. A. Reynolds, and J. S. van Duijneveldt, *J. Chem. Phys.* **117**, 9947 (2002).
  - [121] L. Onsager, *Phys. Rev.* **62**, 558, (1942).
  - [122] L. Onsager, *Ann. (N.Y.) Acad. Sci.* **51**, 627 (1949).
  - [123] J. D. Parsons, *Phys. Rev. A* **19**, 1225 (1979).
  - [124] S. D. Lee, *J. Chem. Phys.* **87**, 4972 (1987).
  - [125] S. D. Lee, *J. Chem. Phys.* **89**, 7036 (1989).
  - [126] H. H. Wensink, *Liquid Crystal Phase Behavior of Colloidal Mixtures*, PhD thesis, University of Utrecht (2004).
  - [127] H. N. W. Lekkerkerker, W. C. K. Poon, P. N. Pusey, A. Stoobants, and P. Warren, *Europhys. Lett.* **20**, 559 (1992).
  - [128] Y. Rosenfeld, *J. Chem. Phys.* **89**, 4272 (1988).
  - [129] Y. Rosenfeld and P. Tarazona, *Molec. Phys.* **95**, 141 (1998).
  - [130] P. Tarazona and Y. Rosenfeld, *Phys. Rev. E* **55**, 4873(R) (1997).
  - [131] B. Barboy and W. M. Gelbart, *J. Chem. Phys.* **71**, 3053 (1979).
  - [132] B. Barboy and W. M. Gelbart, *J. Stat. Phys.* **22**, 709 (1980).
  - [133] L. Harnau, D. G. Rowan, and J.-P. Hansen, *J. Chem. Phys.* **117**, 11359 (2002).
  - [134] L. Harnau and S. Dietrich in *Soft Matter*, edited G. Gompper and M. Schick, Vol. 3 p. 159, (Wiley-VCH, Berlin, 2007).
  - [135] R. Evans in *Fundamentals of Inhomogeneous Fluids*, edited D. Henderson, p. 85, (Dekker, New York, 1992).
  - [136] J. Wu, *AIChE Journal* **52**, 1169 (2006).
  - [137] A. Esztermann, H. Reich, and M. Schmidt, *Phys. Rev. E* **73**, 011409 (2006).
  - [138] L. Harnau and S. Dietrich, *Phys. Rev. E* **65**, 021505 (2002).
  - [139] H. Reich, M. Dijkstra, R. van Roij, and M. Schmidt, *J. Phys. Chem. B* **111**, 7825 (2007).
  - [140] H. Reich and M. Schmidt, *J. Phys.: Condens. Matter* **19**, 326103 (2007).
  - [141] C. G. Maitland, *Curr. Opin. Colloid Interface Sci.* **5**, 301 (2000).
  - [142] A. C. Perdigon-Aller, M. Aston and S. M. Clarke, *J. Colloid Interface Sci.* **290**, 155 (2005).
  - [143] Y. Rosenfeld, *Phys. Rev. E* **50**, 3318(R) (1994).
  - [144] Y. Rosenfeld, *Molec. Phys.* **86**, 637 (1995).
  - [145] Y. Rosenfeld, *J. Phys.: Condens. Matter* **8**, 9289 (1996).
  - [146] J. Kolafa and M. Rottner, *Molec. Phys.* **104**, 3435 (2006).
  - [147] L. L. Rasmussen and D. W. Oxtoby, *J. Phys.: Condens. Matter* **14**, 12021 (2002).
  - [148] M. Piech and J. Y. Walz, *J. Colloid Interface Sci.* **232**, 86 (2000).
  - [149] S. M. Oversteegen and H. N. W. Lekkerkerker, *Phys. Rev. E* **68**, 021404 (2003).
  - [150] L. Harnau and S. Dietrich, *Phys. Rev. E* **69**, 051501 (2004).
  - [151] S. M. Oversteegen and H. N. W. Lekkerkerker, *Physica A* **341**, 23 (2004).
  - [152] S. M. Oversteegen and H. N. W. Lekkerkerker, *J. Chem. Phys.* **120**, 2470 (2004).
  - [153] L. Harnau and S. Dietrich, *Phys. Rev. E* **71**, 011504 (2005).
  - [154] S. M. Oversteegen, C. Vonk, J. E. G. J. Wijnhoven, and H. N. W. Lekkerkerker, *Phys. Rev. E* **71**, 041406 (2005).
  - [155] T. G. Mason, *Phys. Rev. E* **66**, 060402 (2002).
  - [156] K. Zhao and T. G. Mason, *Phys. Rev. Lett.* **99**, 268301 (2007).
  - [157] R. Zwanzig, *J. Chem. Phys.* **39**, 1714 (1963).
  - [158] L. Harnau, D. G. Rowan, and J.-P. Hansen, *J. Chem. Phys.* **117**, 11359 (2002).
  - [159] J. A. Cuesta, *Phys. Rev. Lett.* **76**, 3742 (1996).
  - [160] J. A. Cuesta and Y. Martínez-Ratón, *Phys. Rev. Lett.* **78**, 3681 (1997).
  - [161] J. A. Cuesta and Y. Martínez-Ratón, *J. Chem. Phys.* **107**, 6379 (1997).
  - [162] D. G. Rowan and J.-P. Hansen, *Phys. Chem. Chem. Phys.* **4**, 3390 (2002).
  - [163] L. Harnau and S. Dietrich, *Phys. Rev. E* **66**, 051702 (2002).
  - [164] M. Bier, L. Harnau and S. Dietrich, *Phys. Rev. E* **69**, 021506 (2004).
  - [165] D. van der Beek, H. Reich, P. van der Schoot, M. Dijkstra, T. Schilling, R. Vink, M. Schmidt, R. van Roij, and H. N. W. Lekkerkerker, *Phys. Rev. Lett.* **97**, 087801 (2006).
  - [166] R. van Roij and B. Mulder, *J. Phys. II France* **4**, 4089 (1994).
  - [167] E. Sokolova and A. Vlasov, *J. Phys. Condens. Matter* **9**, 4089 (1997).
  - [168] Y. Martínez-Ratón and J. A. Cuesta, *Phys. Rev. Lett.* **89**, 185701 (2002).
  - [169] L. Harnau, F. Penna, and S. Dietrich, *Phys. Rev. E* **70**, 021505 (2004).
  - [170] M. Bier and R. van Roij, *Phys. Rev. E* **76**, 021405 (2007).
  - [171] M. Bier and R. van Roij, *Phys. Rev. E* **77**, 021401 (2008).
  - [172] M. Bier, L. Harnau and S. Dietrich, *J. Chem. Phys.* **123**, 114906 (2005).
  - [173] M. Bier, L. Harnau and S. Dietrich, *J. Chem. Phys.* **125**, 184704 (2006).
  - [174] Y. Martínez-Ratón and J. A. Cuesta, *J. Chem. Phys.* **118**, 10164 (2003).
  - [175] Y. Martínez-Ratón, *Phys. Rev. E* **69**, 061712 (2004).
  - [176] Y. Martínez-Ratón, *Phys. Rev. E* **75**, 051708 (2007).
  - [177] B. S. John and F. A. Escobedo, *J. Phys. Chem. B* **109**, 23008 (2005).
  - [178] A. V. Petukhov, D. van der Beek, R. P. A. Dullens, I. P. Dolbnya, G. J. Vroege, H. N. W. Lekkerkerker, *Phys. Rev. Lett.* **95**, 077801 (2005).
  - [179] J. A. Capitán and J. A. Cuesta, *Phys. Rev. E* **76**, 011403 (2007).

[180] H. H. Wensink, Phys. Rev. Lett. **93**, 157801 (2004).

[181] G.-Z. Lai, C.-X. W, abd Y.-P Xue, Molec. Cryst. Liq.

Cryst. **460**, 35 (2006).